Benchmarking Quantum Simulators using Quantum Chaos

Daniel K. Mark, Joonhee Choi, Adam L. Shaw, Manuel Endres, and Soonwon Choi, *

Center for Theoretical Physics, Massachusetts Institute of Technology, Cambridge, MA 02139, USA

California Institute of Technology, Pasadena, CA 91125, USA

We propose and analyze a sample-efficient protocol to estimate the fidelity between an experimentally prepared state and an ideal target state, applicable to a wide class of analog quantum simulators without advanced sophisticated spatiotemporal control. Our approach utilizes newly discovered universal fluctuations emerging from generic Hamiltonian dynamics, and it does not require any fine-tuned control over state preparation, quantum evolution, or readout capability. It only needs a small number of experimental measurements, achieving near optimal sample complexity: in ideal cases, a percent-level precision is obtained with $\sim 10^3$ measurements independent of system size. Furthermore, the accuracy of our fidelity estimation improves with increasing system size. We numerically demonstrate our protocol for a variety of quantum simulator platforms such as itinerant particles on optical lattices, trapped ions, and Rydberg atoms. We discuss further applications of our method for advanced tasks such as multi-parameter estimation of quantum states and processes.

Introduction.—Recent advances in quantum technology have opened up new ways to probe quantum manybody physics, leading to the first observations of novel phases of matter [1-5], quantum thermalization [6-8], and various exotic non-equilibrium phenomena [9–14]. However, in order to advance to the next stage of quantum simulation producing highly accurate data, it is important to quantify the performance of a quantum device. One such task is quantum device benchmarking [15] verifying that a quantum hardware accurately produces a desired state in the presence of imperfections and noise, measured by the fidelity $F = \langle \Psi_{\rm ideal} | \rho_{\rm exp} | \Psi_{\rm ideal} \rangle$ between a target state $|\Psi_{\rm ideal}\rangle$ and an experimentally prepared state ρ_{exp} . A high fidelity certifies that any property of the produced state is close to that of the target state. Hence, the fidelity is widely used in theory to quantify the goodness of state preparation or operations [16], and its measurement in the laboratory is important for building increasingly complex and highly precise systems.

Several methods to benchmark quantum devices have been proposed. A naïve approach is to perform quantum state tomography [16-19], in which an experimental state is fully characterized by measurements in many different bases. This approach, however, is impractical even for relatively small quantum systems as it requires prohibitively many measurements. Alternatively, recent proposals pointed out that one can estimate the fidelity from a small number of measurements performed in a set of randomly chosen bases [20-27]. These methods, generally referred to as randomized measurements [24], rely on implementing highly engineered quantum gates that satisfy certain statistical properties. These methods are not readily applicable to a range of quantum devices with limited controllability. In particular, analog quantum simulators are often designed to realize specific forms of many-body Hamiltonians and lack the ability to implement sophisticated operations. In contrast, most existing benchmarking protocols require time-dependent, local controls [28, 29] or the measurement of many different

observables [30–33], hence they are challenging to implement. Very recently, a method based on generic quantum dynamics has been developed and demonstrated [34], yet the method works only for the quench dynamics of an initial state at infinite effective temperature without any symmetries, limiting its application for generic systems. Thus, it is of great interest to develop a general approach to benchmark quantum simulators, demanding as minimal hardware capabilities as possible.

In this work, we propose and analyze a benchmarking protocol that requires minimal control in experiment: one prepares an initial state, time-evolves it under a natural Hamiltonian of the system, and performs measurements in a fixed basis. We show that for generic quantum systems, a small number of such measurements are already sufficient to estimate the fidelity F, which encapsulates the combined effects of errors in the state preparation, unitary evolution, and readout steps. Importantly, our method works with quench dynamics at finite effective temperature, in the presence of symmetries, and for non-qubit based systems such as itinerant particles on optical lattices, making it a general approach applicable for a wide class of existing platforms.

The ability to estimate fidelity forms a working basis for two desired tasks: (i) target state benchmarking, where the overlap between an experimentally prepared state and a pure target state is measured by time evolving those states under a quench Hamiltonian with high fidelity, and (ii) quantum process benchmarking, where the fidelity decay of generic Hamiltonian dynamics is monitored as a function of evolution time.

Our benchmarking protocol is inspired by a previously introduced method, based on two principles: universal statistical fluctuations and operator scrambling that occur in random unitrary circuits (RUCs) [36–38]. We show that the same universal statistics are present even in realistic Hamiltonian dynamics, after appropriate data processing in our protocol. The ability to estimate the fidelity leads to further applications such as multi-

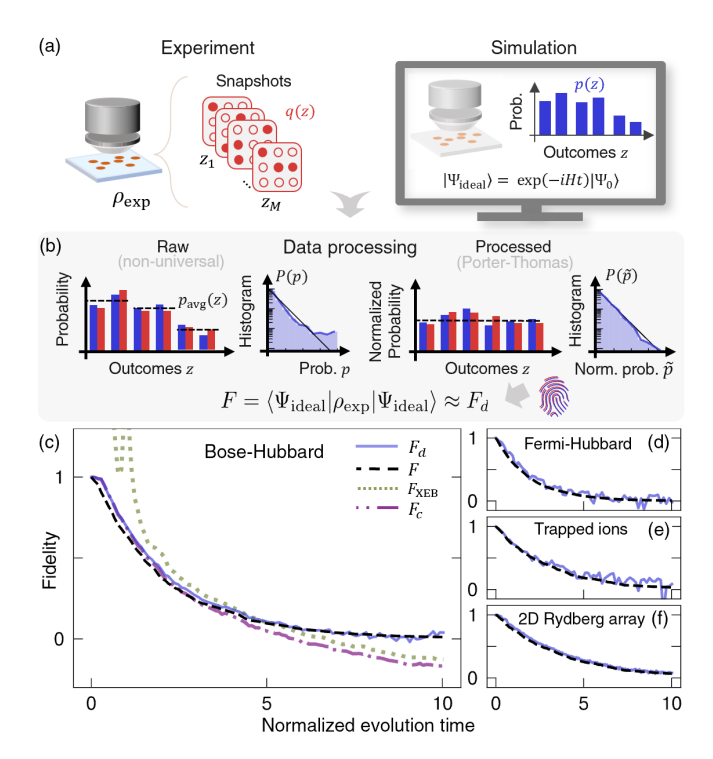


FIG. 1. Schematic of benchmarking protocol. (a) Measurement snapshots $\{z_1, \ldots, z_M\}$ drawn from a distribution q(z), associated with an experimentally prepared state $\rho_{\rm exp}$, are compared against the theoretical probability distribution p(z) associated with an ideal pure state $|\Psi_{\text{ideal}}\rangle$. (b) The raw distributions p(z) and q(z) (blue and red bars, left) fluctuate about systematic average values $p_{\text{avg}}(z)$ (dashed lines), giving rise to a non-universal histogram of probabilities. Via proper normalization, these systematic averages are eliminated, leaving only the fluctuations in the processed distribution $\tilde{p}(z)$. These form a speckle pattern that approximately follows the universal Porter-Thomas distribution (right). F_d estimates the overlap fidelity F between ρ_{exp} and $|\Psi_{\text{ideal}}\rangle$, by comparing the speckle patterns that serve as fingerprints of the quantum state. (c) F_d closely tracks the decay of fidelity F (black dashed) between noisy and ideal quench dynamics as a function of evolution time in a 1D Bose-Hubbard model. In contrast, previously proposed benchmarks F_{XEB} (green dotted) or F_c (purple dot-dashed) show significant deviations due to the finite effective temperature of the initial state we consider. (d-f) Our method is applicable to a wide class of analog simulators including an integrable 1D Fermi-Hubbard model, a trapped-ion model, and a 2D Rydberg array at finite effective temperature, see SM [35] for simulation details.

parameter estimation of quantum states and Hamiltonians, which we demonstrate numerically.

Protocol.—Our protocol consists of three basic steps: experiment, simulation, and data processing. See Table I and Fig. 1(a,b). In the experiment, the initial state can either be an easy-to-prepare fiducial state or a more complex state that one wishes to benchmark. After quench evolution for time t, measurements can be done in the most natural basis $\{|z\rangle\}$ of a given hardware, as long as all possible measurement outcomes form a complete basis, e.g. particle number configurations in quantum gas

TABLE I. Proposed benchmarking protocol

Experiment:

- 1. Prepare an initial state $|\Psi_0\rangle$.
- 2. Evolve the system under its natural Hamiltonian H for time t.
- 3. Measure the evolved state $\rho(t)$ in a natural basis to obtain configurations $\{z_j\}_{j=1}^M$.

Simulation: Classically compute:

- 1. $p(z,t) \equiv |\langle z| \exp(-iHt) |\Psi_0\rangle|^2$,
- 2. $p_{\text{avg}}(z) \equiv \lim_{T \to \infty} \frac{1}{T} \int_0^T p(z, t) dt$,
- 3. $\tilde{p}(z,t) = p(z,t)/p_{\text{avg}}(z)$.

Data processing: Evaluate an unbiased estimator,

$$\hat{F}_d \equiv rac{2}{\sum_z p_{
m avg}(z) ilde{p}(z,t)^2} \left[rac{1}{M} \sum_{i=1}^M ilde{p}(z_i,t)
ight] - 1 \; ,$$

for our benchmark F_d in Eq. (1), which approximates the fidelity $F = \langle \Psi_0 | e^{iHt} \rho(t) e^{-iHt} | \Psi_0 \rangle$.

microscopes. Repeating M times, one measures configurations $\{z_1, \ldots, z_M\}$, where each z_i is sampled from the probability distribution $q(z,t) \equiv \langle z | \rho(t) | z \rangle$.

Classically simulating the same process gives the theoretical distribution p(z,t) and its infinite time-average $p_{\text{avg}}(z)$ [39]. In practice, one may approximate $p_{\text{avg}}(z)$ by averaging p(z,t) over a finite duration.

Finally, we compare the experimental data and theory predictions by using our benchmark

$$F_d(t) \equiv 2 \frac{\sum_z p_{\text{avg}}(z) \tilde{q}(z, t) \tilde{p}(z, t)}{\sum_z p_{\text{avg}}(z) \tilde{p}(z, t)^2} - 1 , \qquad (1)$$

where $\tilde{p}(z,t)$ and $\tilde{q}(z,t) \equiv q(z,t)/p_{\rm avg}(z)$ are normalized outcome probabilities from theory and experiment respectively. F_d can be efficiently evaluated by using the unbiased estimator in Table I, and we analyze the number of requisite samples below. We claim that F_d approximates the fidelity F for a wide class of quantum systems, when the amount of error is reasonably small and not strongly correlated [35, 40–42].

Figure 1(c-f) numerically demonstrates our quantum process benchmarking, where F_d indeed successfully traces the fidelity decay in four different quantum simulation platforms. For each platform, we consider the system initialized in a simple product state, undergoing its natural Hamiltonian dynamics with realistic parameters in the presence of experimentally relevant errors [35]. We also present numerical demonstrations of target state benchmarking in the Supplementary Material (SM) [35].

Speckle-based benchmarking.—The salient and surprising feature of our protocol is that the fidelity can be estimated from measurement data obtained in a fixed basis, despite the fact that the state overlap depends on phase information inaccessible from these measurements. Indeed, an instantaneous phase error may change F but not F_d . Nevertheless, we will show that, owing to the combination of operator scrambling and emergent universal

statistics, F_d still approximates F for generic quantum states produced in our protocol.

To see this, we briefly review the qualitative mechanism of a previous approach: the linear cross-entropy benchmark (XEB) [36] $F_{\rm XEB}\equiv D\sum_z q(z)p(z)-1$ estimates the fidelity of running RUCs on an N-qubit system with Hilbert space dimension D. When a typical output state from a deep RUC is measured, its outcome distribution p(z) is not perfectly uniform, but exhibits a speckle pattern: over different z's, p(z) fluctuates around 1/Ddue to random interference from coherent quantum dynamics. While the detailed pattern of the fluctuations — which p(z)'s are relatively larger — sensitively depends on the choice of a particular RUC, the amount of fluctuation is universal: $\sum_{z} p^{2}(z) \approx 2/D$. In fact, all statistical properties of $\{p(z)\}_z$ are universal: viewing p(z)for each z as an independent sample of a random variable, $\{p(z)\}_z$ follows the so-called Porter-Thomas (PT) distribution [35, 36].

Crucially, the speckle pattern may serve as a fingerprint of a quantum state since any local error drastically changes the pattern with high probability. When an error occurs in chaotic dynamics, its subsequent time evolution scrambles the error operator into a complicated nonlocal form [37, 38]. This operator scrambling allows for the detection of even phase errors, which are diagonal in the measurement basis. The scrambled operator leads to a new probability: $q(z) = Fp(z) + (1 - F)p_{\perp}(z)$ where the second term is uncorrelated with the original pattern, $\sum_{z} p(z)p_{\perp}(z) \approx 1/D$ with high probability [41]. In fact, as a function of time after the error, it is exponentially unlikely that p_{\perp} and p are correlated [40]. Then, it follows from the universal fluctuation that $F_{XEB} = F + O(1/D)$. It has been rigorously shown that the XEB approximates the fidelity for deep RUCs as long as errors are sufficiently weak (or occur sparsely) and uncorrelated [40–43].

For shallow circuits, however, the XEB is not applicable since the resultant $\{p(z)\}_z$ does not exhibit such universal fluctuations. Recently this limitation was alleviated by a new formula $F_c \equiv 2\sum_z q(z)p(z)/\sum_z p(z)^2 - 1$ [34]. The key idea is that, even for relatively short time evolution, universal fluctuations can still emerge locally in the conditional distribution of local measurement outcomes under certain conditions such as shallow RUCs or chaotic Hamiltonian dynamics at infinite effective temperature without any symmetries [34, 44].

Emergent universal statistics— Under realistic Hamiltonian evolution away from infinite temperature, the universal PT distribution is not obtained either globally or locally. The presence of energy conservation or other symmetries leads to certain systematic patterns in $\{p(z)\}_z$, distorting its distribution away from PT. For example, for any state with positive effective temperature, low-energy configurations are more likely to be measured. Similarly, the presence of symmetries may bias measure-

ment outcome distributions [35]. For this reason, F_{XEB} or F_c deviates from F in generic quantum simulators as shown in Fig. 1(c).

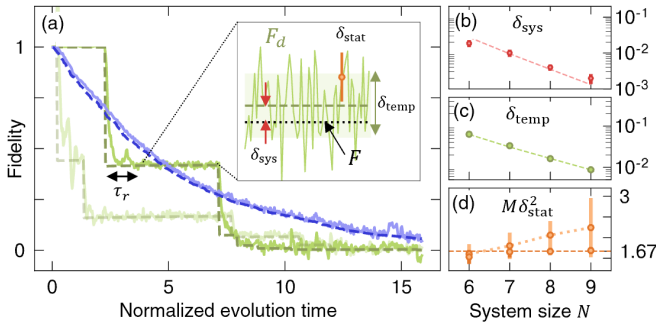
Our generalized benchmarking protocol is enabled by a new finding: in spite of nonuniversal systematic patterns in $\{p(z)\}_z$, universal statistics can be recovered via appropriate data processing. Specifically, the systematic deviation is captured by the time-averaged factor $p_{\text{avg}}(z)$. Hence, normalizing p(z) with $p_{\text{avg}}(z)$ leaves only random fluctuations, unveiling the desired statistical properties. This is described by the following theorem.

Theorem. (informal) Consider an initial state $|\Psi_0\rangle$ and a Hamiltonian H satisfying the k-th no-resonance condition for a large integer k. Then, the normalized probabilities $\tilde{p}(z) \equiv p(z)/p_{avg}(z)$ approximately follow the Porter-Thomas distribution at late times, up to a correction bounded by the effective Hilbert space dimension D_{β} , where $D_{\beta}^{-1} \equiv \sum_{z,E} |\langle z|E\rangle|^4 |\langle E|\Psi_0\rangle|^4/p_{avg}(z)$ and $\{|E\rangle\}$ are the energy eigenstates of H.

A similar statement holds for $\tilde{p}(z,t)$'s with a fixed z evaluated at different evolution times. A rigorous statement of our Theorem as well as its proof are presented in the SM [35]. Our theorem only relies on the k-th no-resonance condition, which states that the eigenvalues $\{E_j\}$ of H possess no resonant structures. That is, $\sum_{i=1}^k E_{\alpha_i} = \sum_{i=1}^k E_{\beta_i}$ if and only if the k indices (α_i) are a permutation of (β_i) [45–49]. This no-resonance condition is expected to hold for generic ergodic Hamiltonians [45, 46]. The effective Hilbert space dimension D_{β} quantifies the degree of ergodicity of the quench evolution, and is generically exponentially large in system size, enabling high accuracy in our protocol. We note that the required k-th no-resonance condition is weaker than demanding the ergodicity of H in its full Hilbert space; some interacting integrable systems satisfy this condition. Thus, our protocol is applicable even for such systems, as demonstrated with a 1D Fermi-Hubbard model at half-filling in Fig. 1(c), which is an interacting integrable model [35, 50].

Our benchmark F_d utilizes these universal properties to estimate F in the same way as F_{XEB} and F_c . For example, assuming an ansatz $\tilde{q}(z) = F\tilde{p}(z) + (1-F)\tilde{p}_{\perp}(z)$, the relation $F_d \approx F$ can be easily shown. Moreover, F_d reduces to F_c and F_{XEB} under appropriate limiting cases, such as quench dynamics at infinite effective temperature. In fact, we can relax the above ansatz and still prove $F_d \approx F$ by using the Eigenstate Thermalization Hypothesis and the k-th no-resonance condition at late times [35, 51]. From extensive numerical simulations, we have also found that $F_d \approx F$ holds even for relatively short quench evolution well before the PT distribution emerges from the global probabilities, similar to the case of F_c [Fig. 1(c,d) and SM] [34].

Performance. — Having established the working principles of F_d , we proceed to characterize its performance.



Detailed analysis of our benchmarking protocol. (a) We simulate open quantum dynamics of a 1D Bose-Hubbard model with N particles on N sites based on the stochastic wavefunction method [52] and analyze individual quantum trajectories (green) corresponding to specific occurrences of errors. In each trajectory, F_d (solid line) closely agrees with the fidelity F (dashed line). It takes a short delay time τ_r for F_d to approach F (black arrow). Averaging F_d and Facross all trajectories gives their overall values for the mixed state ρ (blue line). Inset: Even after τ_r , our benchmark F_d may slightly deviate from F owing to a systematic difference δ_{sys} between F and the time-averaged F_d (red arrow) and the fluctuation δ_{temp} of F_d over time (green arrow). When F_d is estimated from a finite number of samples M, the unbiased estimator \hat{F}_d [Table I] (orange marker) has a statistical uncertainty δ_{stat} (error bar) (b,c) Both δ_{sys} and δ_{temp} decrease exponentially with system size, up to N = 9 studied here (corresponding to a Hilbert space dimension of 24310), consistent with our analytic prediction (dashed lines). (d) The sample complexity $M\delta_{\mathrm{stat}}^2$ increases weakly with N at early times (dotted line). At late times, however, it approaches an N-independent, universal value (dashed line). Error bars in (b-d) indicate the fluctuations over an ensemble of disordered Hamiltonians. See SM [35] for details.

We first show that it suffices to study the effect of a single error. As a representative example, we consider noisy dynamics of the Bose-Hubbard model. We investigate the evolution of a mixed state by unravelling it into an ensemble of stochastic pure state trajectories [52], where each trajectory corresponds to a fixed occurrence of errors. When a single error occurs, the fidelity decreases instantly, and F_d follows this decrease after a short time [Fig. 2(a), green]. This delay time τ_r arises from the time needed for an error to be scrambled such that it can be detected in a fixed measurement basis. Averaging over trajectories gives the overall fidelity and F_d of the mixed state dynamics [Fig. 2(a), blue]. As long as the error rates are sufficiently small, the presence of multiple errors does not lead to a qualitatively different behavior [40, 41]. The finite delay time may lead to a slight overestimation of the fidelity when it decays continuously over time [35, 40, 53]; this may be corrected by careful characterization of τ_r .

Given a single error, we quantify the performance of our benchmark along three different axes: systematic errors, temporal fluctuations, and statistical fluctuations. The systematic error $\delta_{\rm sys}$ refers to the difference between the true fidelity and our benchmark averaged over time.

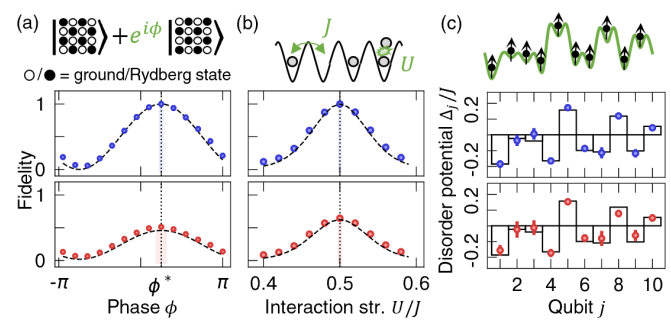


FIG. 3. Estimating unknown parameters of a quantum state or Hamiltonian based on F_d : (a) the phase ϕ for a GHZ-like initial state in a 2D Rydberg system; (b) the normalized interaction strength, U/J, for a 1D Bose-Hubbard model where U and J are the interaction and tunneling strengths; and (c) ten disordered on-site potentials in a trapped ion model. The parameters are estimated by maximizing \hat{F}_d over simulated parameters, assuming error-free (blue, middle row) or noisy (red, bottom row) quench evolution. The error bars and shaded regions indicate the statistical uncertainty in \hat{F}_d and the estimated parameter values when 1000 samples are used. See SM for simulation details. (a,b) Both F (black lines) and \hat{F}_d (marker) are consistent with each other and simultaneously maximized at the true parameter value (dotted line) (c) All ten disorder potential values are approximately reconstructed.

The temporal fluctuation δ_{temp} quantifies the fluctuation of our benchmark in time. The statistical fluctuation δ_{stat} measures the standard deviation of the unbiased estimator \hat{F}_d associated with a finite number of samples M, which determines the so-called sample complexity $M\delta_{\text{stat}}^2$ [Fig. 2(a) inset]. See SM [35] for explicit definitions of these quantities.

For quench Hamiltonians satisfying the k-th noresonance conditions, our Theorem enables us to analytically estimate the size of these errors and fluctuations [35]: we find that both $\delta_{\rm sys}$ and $\delta_{\rm temp}$ are $O(D_{\beta}^{-1})$ and $O(D_{\beta}^{-1/2})$ respectively, determined by the correction term in our Theorem. This implies that both the accuracy and precision of our benchmark improve exponentially with increasing system size. We explicitly confirm this scaling in our numerical simulations [Fig. 2(b,c)].

The sample complexity $M\delta_{\rm stat}^2$ depends on the duration of the quench time and generally decreases (improves) for longer evolution. In the limit of long evolution, we find $M\delta_{\rm stat}^2\approx 1+2F-F^2$, independent of system size [Fig. 2(d), dashed line]. This sample complexity shows an optimal system-size scaling and is equal to that of the best known approach based on randomized measurements [27]. For relatively short time evolution, the sample complexity grows weakly with system size [Fig. 2(d), dotted line].

Limitations.— While our protocol is applicable to generic quantum many-body systems, it may fail in some special cases, which we briefly enumerate. See SM for details and potential resolutions. First, the violation of the

no-resonance conditions may occur in a class of Hamiltonians such as non-interacting itinerant particles or systems with particle-hole symmetry (PHS). Second, if the effective Hilbert space dimension D_{β} is too small, e.g. for low-temperature quenches or dynamics in many-body localized phases [54, 55], both the systematic error and temporal fluctuation may be large. Third, dynamics with particularly slow equilibration compared to error rates, e.g. due to quantum many-body scarring, may lead to the breakdown of our analysis based on isolated single errors. Finally, we comment on the effect of non-local or correlated errors, whose analysis remains challenging even for theory models based on RUCs. Using a novel analysis based on random matrix product states [35, 56], we find that the validity of $F_d \approx F$ undergoes a crossover as a function of the spatial extent of an error: when the size of an error exceeds what we call an entanglement correlation length, F_d may not accurately approximate F. This leads us to design a slightly modified benchmark F_e , which alleviates some of the aforementioned limitations — systems with a relatively small D_{β} , the presence of nonlocal or correlated errors, or PHS — at the expense of having worse performance for short quenches [35].

Additionally, classically simulating exact quench dynamics can be computationally demanding for large systems, limiting the applicability of our method. This challenge can be mitigated by using tensor-network based algorithms. A state-of-the-art method allows exact evaluations of p(z) for RUCs on a 56-qubit system within minutes [57]. Also, approximate algorithms, in combination with Monte Carlo sampling, may be used for 1D or 2D systems with short quench dynamics [58, 59].

Applications.— The ability to measure the fidelity enables further applications. As examples, here we show that one can estimate multiple parameters of quantum states or Hamiltonians, in-situ and simultaneously. The key observation is that, given the ability to measure the fidelity between a theory prediction and experimental data, one can variationally optimize parameters in theory to maximize the estimated fidelity [34, 60]. This optimization process does not necessitate any further data acquisition.

Figure 3 shows the numerical demonstration of this idea for (i) measuring the phase ϕ in a GHZ-like state $|\uparrow\downarrow\uparrow\cdots\rangle + \exp(i\phi)|\downarrow\uparrow\downarrow\cdots\rangle$ by quench evolving the state of interest under a 2D Rydberg blockaded model, (ii) identifying the interaction strength in a Bose-Hubbard model, and (iii) simultaneously determining ten disordered, on-site potentials in a spin chain model (see SM for details [35]). We find the optimized parameters approximately match the true values even when the quench evolutions are noisy, demonstrating the robustness of this approach.

Conclusion and Outlook.—We present a new protocol to efficiently estimate the fidelity of quantum states produced in a variety of analog quantum simulators, which

requires no fine-tuned control and hence is easy to implement with existing technology. Our benchmarking method is an example of a quantum application based on the emergence of certain universal features of generic Hamiltonian dynamics. We anticipate further protocols of this kind for applications such as quantum metrology, or quantum state and process learning.

Acknowledgments.— We would like to thank Wen Wei Ho, Anant Kale, Eun Jong Kim, Sherry Zhang, and Peter Zoller for useful discussions. In particular, we thank Sherry Zhang for a careful read of this manuscript and Anant Kale for insightful discussion at the early stage of the project. We acknowledge funding provided by the Institute for Quantum Information and Matter, an NSF Physics Frontiers Center (NSF Grant PHY 1733907), the NSF CAREER award (1753386), the AFOSR YIP (FA9550-19-1-0044), the DARPA ONISQ program (W911NF2010021), the Army Research Office MURI program (W911NF2010136), the NSF QLCI program (2016245), and the DOE (DE-SC0021951). JC acknowledges support from the IQIM postdoctoral fellowship. ALS acknowledges support from the Eddleman Quantum graduate fellowship.

* soonwon@mit.edu

- M. Greiner, O. Mandel, T. Esslinger, T. W. Hänsch, and I. Bloch, Quantum phase transition from a superfluid to a Mott insulator in a gas of ultracold atoms, Nature (London) 415, 39 (2002).
- [2] M. Aidelsburger, M. Atala, M. Lohse, J. T. Barreiro, B. Paredes, and I. Bloch, Realization of the Hofstadter Hamiltonian with ultracold atoms in optical lattices, Phys. Rev. Lett. 111, 185301 (2013).
- [3] G. Jotzu, M. Messer, R. Desbuquois, M. Lebrat, T. Uehlinger, D. Greif, and T. Esslinger, Experimental realization of the topological Haldane model with ultracold fermions, Nature (London) 515, 237 (2014).
- [4] C. Gross and I. Bloch, Quantum simulations with ultracold atoms in optical lattices, Science 357, 995 (2017).
- [5] S. Ebadi, T. T. Wang, H. Levine, A. Keesling, G. Semeghini, A. Omran, D. Bluvstein, R. Samajdar, H. Pichler, W. W. Ho, et al., Quantum phases of matter on a 256-atom programmable quantum simulator, Nature (London) 595, 227 (2021).
- [6] A. M. Kaufman, M. E. Tai, A. Lukin, M. Rispoli, R. Schittko, P. M. Preiss, and M. Greiner, Quantum thermalization through entanglement in an isolated manybody system, Science 353, 794 (2016).
- [7] Y. Tang, W. Kao, K.-Y. Li, S. Seo, K. Mallayya, M. Rigol, S. Gopalakrishnan, and B. L. Lev, Thermalization near integrability in a dipolar quantum Newton's cradle, Phys. Rev. X 8, 021030 (2018).
- [8] F. Chen, Z.-H. Sun, M. Gong, Q. Zhu, Y.-R. Zhang, Y. Wu, Y. Ye, C. Zha, S. Li, S. Guo, et al., Observation of strong and weak thermalization in a superconducting quantum processor, Phys. Rev. Lett. 127, 020602 (2021).
- [9] B. Neyenhuis, J. Zhang, P. W. Hess, J. Smith, A. C. Lee,

- P. Richerme, Z.-X. Gong, A. V. Gorshkov, and C. Monroe, Observation of prethermalization in long-range interacting spin chains, Science Adv. 3, e1700672 (2017).
- [10] J. Zhang, G. Pagano, P. W. Hess, A. Kyprianidis, P. Becker, H. Kaplan, A. V. Gorshkov, Z.-X. Gong, and C. Monroe, Observation of a many-body dynamical phase transition with a 53-qubit quantum simulator, Nature (London) 551, 601 (2017).
- [11] J. Choi, H. Zhou, S. Choi, R. Landig, W. W. Ho, J. Isoya, F. Jelezko, S. Onoda, H. Sumiya, D. A. Abanin, et al., Probing quantum thermalization of a disordered dipolar spin ensemble with discrete time-crystalline order, Phys. Rev. Lett. 122, 043603 (2019).
- [12] A. Rubio-Abadal, M. Ippoliti, S. Hollerith, D. Wei, J. Rui, S. Sondhi, V. Khemani, C. Gross, and I. Bloch, Floquet prethermalization in a Bose-Hubbard system, Phys. Rev. X 10, 021044 (2020).
- [13] P. Peng, C. Yin, X. Huang, C. Ramanathan, and P. Cappellaro, Floquet prethermalization in dipolar spin chains, Nature Physics 17, 444 (2021).
- [14] X. Mi, M. Ippoliti, C. Quintana, A. Greene, Z. Chen, J. Gross, F. Arute, K. Arya, J. Atalaya, R. Babbush, et al., Time-crystalline eigenstate order on a quantum processor, Nature (London), 1 (2021).
- [15] J. Eisert, D. Hangleiter, N. Walk, I. Roth, D. Markham, R. Parekh, U. Chabaud, and E. Kashefi, Quantum certification and benchmarking, Nature Rev. Phys. 2, 382 (2020).
- [16] M. A. Nielsen and I. L. Chuang, Quantum Computation and Quantum Information: 10th Anniversary Edition (Cambridge University Press, 2010).
- [17] M. Cramer, M. B. Plenio, S. T. Flammia, R. Somma, D. Gross, S. D. Bartlett, O. Landon-Cardinal, D. Poulin, and Y.-K. Liu, Efficient quantum state tomography, Nature Comm. 1, 1 (2010).
- [18] D. Gross, Y.-K. Liu, S. T. Flammia, S. Becker, and J. Eisert, Quantum state tomography via compressed sensing, Phys. Rev. Lett. 105, 150401 (2010).
- [19] M. Christandl and R. Renner, Reliable quantum state tomography, Phys. Rev. Lett. 109, 120403 (2012).
- [20] S. T. Flammia and Y.-K. Liu, Direct fidelity estimation from few Pauli measurements, Phys. Rev. Lett. 106, 230501 (2011).
- [21] M. P. da Silva, O. Landon-Cardinal, and D. Poulin, Practical characterization of quantum devices without tomography, Phys. Rev. Lett. 107, 210404 (2011).
- [22] S. Aaronson, Shadow tomography of quantum states, SIAM Journal on Computing 49, STOC18 (2019).
- [23] H.-Y. Huang, R. Kueng, and J. Preskill, Predicting many properties of a quantum system from very few measurements, Nature Physics 16, 1050 (2020).
- [24] A. Elben, B. Vermersch, C. F. Roos, and P. Zoller, Statistical correlations between locally randomized measurements: A toolbox for probing entanglement in many-body quantum states, Phys. Rev. A 99, 052323 (2019).
- [25] A. Elben, B. Vermersch, R. van Bijnen, C. Kokail, T. Brydges, C. Maier, M. K. Joshi, R. Blatt, C. F. Roos, and P. Zoller, Cross-platform verification of intermediate scale quantum devices, Phys. Rev. Lett. 124, 010504 (2020).
- [26] Y. Liu, M. Otten, R. Bassirianjahromi, L. Jiang, and B. Fefferman, Benchmarking near-term quantum computers via random circuit sampling, arXiv:2105.05232 (2021).

- [27] A. Elben, S. T. Flammia, H.-Y. Huang, R. Kueng, J. Preskill, B. Vermersch, and P. Zoller, The randomized measurement toolbox, arXiv:2203.11374 (2022).
- [28] M. Ohliger, V. Nesme, and J. Eisert, Efficient and feasible state tomography of quantum many-body systems, N. J. Phys. 15, 015024 (2013).
- [29] T. Brydges, A. Elben, P. Jurcevic, B. Vermersch, C. Maier, B. P. Lanyon, P. Zoller, R. Blatt, and C. F. Roos, Probing Rényi entanglement entropy via randomized measurements, Science 364, 260 (2019).
- [30] Z. Li, L. Zou, and T. H. Hsieh, Hamiltonian tomography via quantum quench, Phys. Rev. Lett. 124, 160502 (2020).
- [31] C. Kokail, R. van Bijnen, A. Elben, B. Vermersch, and P. Zoller, Entanglement hamiltonian tomography in quantum simulation, Nature Physics 17, 936 (2021).
- [32] M. Gluza and J. Eisert, Recovering quantum correlations in optical lattices from interaction quenches, Phys. Rev. Lett. 127, 090503 (2021).
- [33] H.-Y. Hu, S. Choi, and Y.-Z. You, Classical shadow tomography with locally scrambled quantum dynamics, arXiv:2107.04817 (2021).
- [34] J. Choi, A. L. Shaw, I. S. Madjarov, X. Xie, J. Covey, J. Cotler, D. K. Mark, H.-Y. Huang, A. Kale, H. Pichler, F. G. Brandão, S. Choi, and M. Endres, Emergent randomness and benchmarking from many-body quantum chaos, arXiv:2103.03535 (2021).
- [35] See Supplemental material online for the proof of our theorem, detailed analysis of the performance, numerical demonstration, and limitations of our protocol, which includes Refs. [44, 61–66].
- [36] S. Boixo, S. V. Isakov, V. N. Smelyanskiy, R. Babbush, N. Ding, Z. Jiang, M. J. Bremner, J. M. Martinis, and H. Neven, Characterizing quantum supremacy in nearterm devices, Nature Physics 14, 595 (2018).
- [37] A. Nahum, S. Vijay, and J. Haah, Operator spreading in random unitary circuits, Phys. Rev. X 8, 021014 (2018).
- [38] V. Khemani, A. Vishwanath, and D. A. Huse, Operator spreading and the emergence of dissipative hydrodynamics under unitary evolution with conservation laws, Phys. Rev. X 8, 031057 (2018).
- [39] This is equivalent to the bitstring probability distribution obtained from a diagonal ensemble $\rho_d \equiv \lim_{T\to\infty} \frac{1}{T} \int_0^T |\Psi(t)\rangle\langle\Psi(t)| \, dt$. [40] X. Gao, M. Kalinowski, C.-N. Chou, M. D. Lukin,
- [40] X. Gao, M. Kalinowski, C.-N. Chou, M. D. Lukin, B. Barak, and S. Choi, Limitations of linear cross-entropy as a measure for quantum advantage, arXiv:2112.01657 (2021).
- [41] A. M. Dalzell, N. Hunter-Jones, and F. G. S. L. Brandão, Random quantum circuits transform local noise into global white noise, arXiv:2111.14907 (2021).
- [42] K. Noh, L. Jiang, and B. Fefferman, Efficient classical simulation of noisy random quantum circuits in one dimension, Quantum 4, 318 (2020).
- [43] B. Barak, C.-N. Chou, and X. Gao, Spoofing linear crossentropy benchmarking in shallow quantum circuits, arXiv preprint arXiv:2005.02421 (2020).
- [44] J. S. Cotler, D. K. Mark, H.-Y. Huang, F. Hernandez, J. Choi, A. L. Shaw, M. Endres, and S. Choi, Emergent quantum state designs from individual many-body wavefunctions, arXiv:2103.03536 (2021).
- [45] S. Goldstein, J. L. Lebowitz, R. Tumulka, and N. Zanghi, On the distribution of the wave function for systems in

- thermal equilibrium, J. Stat. Phys. 125, 1193 (2006).
- [46] P. Reimann, Foundation of statistical mechanics under experimentally realistic conditions, Phys. Rev. Lett. 101, 190403 (2008).
- [47] N. Linden, S. Popescu, A. J. Short, and A. Winter, Quantum mechanical evolution towards thermal equilibrium, Phys. Rev. E 79, 061103 (2009).
- [48] K. Kaneko, E. Iyoda, and T. Sagawa, Characterizing complexity of many-body quantum dynamics by higherorder eigenstate thermalization, Phys. Rev. A 101, 042126 (2020).
- [49] Y. Huang, Extensive entropy from unitary evolution, arXiv:2104.02053 (2021).
- [50] F. H. Essler, H. Frahm, F. Göhmann, A. Klümper, and V. E. Korepin, *The one-dimensional Hubbard model* (Cambridge University Press, 2005).
- [51] J. M. Deutsch, Eigenstate thermalization hypothesis, Rep. Prog. Phys. 81, 082001 (2018).
- [52] A. J. Daley, Quantum trajectories and open many-body quantum systems, Adv. Phys. 63, 77 (2014).
- [53] X. Mi, P. Roushan, C. Quintana, S. Mandrà, J. Marshall, C. Neill, F. Arute, K. Arya, J. Atalaya, R. Babbush, et al., Information scrambling in quantum circuits, Science 374, 1479 (2021).
- [54] R. Nandkishore and D. A. Huse, Many-body localization and thermalization in quantum statistical mechanics, Annu. Rev. Condens. Matter Phys. 6, 15 (2015).
- [55] D. A. Abanin, E. Altman, I. Bloch, and M. Serbyn, Colloquium: Many-body localization, thermalization, and entanglement, Rev. Mod. Phys. 91, 021001 (2019).
- [56] J. Haferkamp, C. Bertoni, I. Roth, and J. Eisert, Emergent statistical mechanics from properties of disordered random matrix product states, PRX Quantum 2, 040308 (2021).
- [57] X. Liu, C. Guo, Y. Liu, Y. Yang, J. Song, J. Gao, Z. Wang, W. Wu, D. Peng, P. Zhao, F. Li, H.-L. Huang,

- H. Fu, and D. Chen, Redefining the quantum supremacy baseline with a new generation sunway supercomputer, arXiv:2111.01066 (2021).
- [58] S. Paeckel, T. Köhler, A. Swoboda, S. R. Manmana, U. Schollwöck, and C. Hubig, Time-evolution methods for matrix-product states, Ann. Phys. 411, 167998 (2019).
- [59] J. Napp, R. L. La Placa, A. M. Dalzell, F. G. Brandao, and A. W. Harrow, Efficient classical simulation of random shallow 2D quantum circuits, Phys. Rev. X (2019).
- [60] F. Arute, K. Arya, R. Babbush, D. Bacon, J. C. Bardin, R. Barends, R. Biswas, S. Boixo, F. G. Brandão, D. A. Buell, et al., Quantum supremacy using a programmable superconducting processor, Nature (London) 574, 505 (2019).
- [61] A. J. Short, Equilibration of quantum systems and subsystems, N. J. Phys. 13, 053009 (2011).
- [62] S. Sarkar, S. Langer, J. Schachenmayer, and A. J. Daley, Light scattering and dissipative dynamics of many fermionic atoms in an optical lattice, Phys. Rev. A 90, 023618 (2014).
- [63] C. J. Turner, A. A. Michailidis, D. A. Abanin, M. Serbyn, and Z. Papić, Quantum scarred eigenstates in a rydberg atom chain: Entanglement, breakdown of thermalization, and stability to perturbations, Phys. Rev. B 98 (2018).
- [64] C. E. Porter and R. G. Thomas, Fluctuations of nuclear reaction widths, Phys. Rev. 104, 483 (1956).
- [65] H. Bernien, S. Schwartz, A. Keesling, H. Levine, A. Omran, H. Pichler, S. Choi, A. S. Zibrov, M. Endres, M. Greiner, et al., Probing many-body dynamics on a 51-atom quantum simulator, Nature (London) 551, 579 (2017).
- [66] R. Vasseur and J. E. Moore, Nonequilibrium quantum dynamics and transport: from integrability to manybody localization, J. Stat. Mech. 2016, 064010 (2016).

Supplemental Material for: Benchmarking Quantum Simulators using Quantum Chaos

Daniel K. Mark, ¹ Joonhee Choi, ² Adam L. Shaw, ² Manuel Endres, ² and Soonwon Choi ¹ Center for Theoretical Physics, Massachusetts Institute of Technology, Cambridge, MA 02139, USA ² California Institute of Technology, Pasadena, CA 91125, USA

CONTENTS

1.	Emergence of universal statistical properties from Hamiltonian dynamics	2
	A. k-th no-resonance condition	2
	B. k-th no resonance with degeneracies	$\begin{array}{c}2\\2\\2\\4\end{array}$
	C. k-th Hamiltonian twirling identity	2
	D. Porter-Thomas distribution over time	4
	E. Porter-Thomas distribution over outcomes	7
II.	Detailed performance analysis for long quench dynamics	8
	A. Ansatz for how speckle patterns change under errors	9
	B. Systematic error	9
	1. Argument based on Eigenstate Thermalization Hypothesis	10
	C. Variance over time	11
	D. Sample complexity	12
	E. Moderate error rate: Effects of delay time τ_d	12
	F. Large error rate: Critical error rate and operator scrambling time	14
	G. Symmetry Resolution	15
	H. Alternative fidelity estimator F_e	15
III.	Detailed performance analysis for short quench dynamics	16
	A. Overview: random matrix product states	16
	B. Remarks	17
	C. Derivation of result	17
IV.	Details of numerical simulations	18
	A. Bose-Hubbard model	18
	1. Disorder Averaging	18
	B. Fermi-Hubbard model	19
	C. Trapped ion model	19
	D. Rydberg blockaded model	19
V.	Limitations of benchmarking protocol: Failure cases	20
	A. Violating the no-resonance condition: Particle-hole symmetry	20
	1. Real Porter-Thomas distribution	21
	B. Violating the no-resonance condition: Non-interacting models	21
	C. Small effective dimension: Low temperature quench	21
	D. Slow equilibration: Quantum many-body scar states	21
	E. Slow equilibration: Inhomogeneous initial state	22
	F. Non-local error on low entanglement states	23
	G. Non-ergodicity due to symmetry and readout in symmetry-resolved basis	23
VI.	Greedy algorithm for multiparameter estimation	24
	A. Algorithm	24
/II.	Target state benchmarking	24
	A. Coherent local errors	25
	B. Comparing non-locally deformed states	25
	References	27

I. EMERGENCE OF UNIVERSAL STATISTICAL PROPERTIES FROM HAMILTONIAN DYNAMICS

In this section, we present precise statements of our Theorem in the main text and prove them. The significance of our Theorems 1 and 2 is that a Porter-Thomas distribution emerges from measurement outcomes $p(z,t) = |\langle z|\Psi(t)\rangle|^2$ after generic Hamiltonian dynamics, upon appropriate data processing. To prove our theorems, we first establish a new identity, the *k-th Hamiltonian twirling identity*, which only requires one assumption: the eigenvalues of the Hamiltonian *H* satisfy the *k-th no-resonance condition*. We utilize this identity to establish theorems on the emergence of a Porter-Thomas distribution in the normalized measurement outcomes $\tilde{p}(z,t)$.

A. k-th no-resonance condition

Definition (k-th no-resonance): Let E_j be the energy eigenvalues of a Hamiltonian H. H satisfies the k-th no-resonance condition [1-4] if

$$E_{\alpha_1} + E_{\alpha_2} + \dots + E_{\alpha_k} = E_{\beta_1} + E_{\beta_2} + \dots + E_{\beta_k}$$
 (S1)

implies that the indices $(\alpha_1, \alpha_2, \dots, \alpha_k)$ and $(\beta_1, \beta_2, \dots, \beta_k)$ are equal up to reordering. In other words, $\beta_j = \alpha_{\sigma(j)}$ for some permutation $\sigma \in S_k$, where S_k is the group of permutations of k elements (the symmetric group). It is easy to see that if the k-th no-resonance condition is satisfied, then so are the k'-th no-resonance conditions, for k' < k. This assumption is considered generically satisfied: it is believed that if the condition does not hold in a given ergodic system, any small perturbation will generically break any k-th resonances [3].

B. k-th no resonance with degeneracies

The k-th no-resonance conditions are, strictly speaking, violated if the Hamiltonian contains degeneracies: $E_i = E_j, i \neq j$. This violates the first no-resonance condition and so all higher k-th no-resonance conditions. This seems to preclude systems with symmetry-protected degeneracies, which can still be ergodic. For our purposes, however, we will consider pure states $\rho = |\Psi_0\rangle\langle\Psi_0|$. In this case, one can replace any set of degenerate states $\mathcal{E} = \{|\Psi_E\rangle\}$ with a single representative state, defined as the projection of $|\Psi_0\rangle$ onto the degenerate subspace: $\mathcal{P}_{\mathcal{E}} |\Psi_0\rangle$. In this way, all degeneracies are effectively eliminated. Therefore, while Lemma 1 (below) requires the full k-th no-resonance condition, one can modify this condition by demanding the k-th no-resonance condition only after eliminating all degenerates as prescribed above. Our main Theorems only require this weakened version of the k-th no-resonance condition. Hence, our Theorems holds generically even in the presence of degeneracies protected by symmetries.

The k-th no-resonance condition is also notably violated for $k \ge 2$ if there is a particle-hole symmetry, in which the energy spectrum is symmetric about E = 0. This case is discussed in Section V A.

C. k-th Hamiltonian twirling identity

We first present the k-th Hamiltonian twirling identity. This identity is a rewriting of a k-fold quantum channel: we take a state $\rho^{(k)}$ in k-copies of the Hilbert space $\mathcal{H}^{\otimes k}$, and average it over all possible times of time-evolution $U_t^{\otimes k}$ over k copies, with $U_t \equiv \exp(-iHt)$. That is, the channel $C^{(k)}$ is $C^{(k)}[\rho^{(k)}] = \mathbb{E}_t \left[U_t^{\otimes k} \rho^{(k)} U_{-t}^{\otimes k} \right]$ where $\mathbb{E}_t[f(t)] \equiv \lim_{T \to \infty} \frac{1}{T} \int_0^T f(t) dt$ here and below. We dub this the k-th Hamiltonian twirling channel, in analogy to twirling channels, in which a state is averaged over all possible unitaries in a group, most commonly the ensemble of Haar unitaries or the Clifford or Pauli groups [5].

We find that the k-th Hamiltonian twirling channel can be written as sum of (i) a dephasing operator in the energy eigenbasis, followed by a sum of permutations of k elements and (ii) additional terms associated with the double counting of certain permutations. We associate these terms with additional correlations associated with energy conservation, hence we dub these "energy-conservation terms".

Such a rewriting is motivated by *Haar-unitary twirling channels*, which can be written as a sum of permutations [6]. In our Theorem below, we consider a specific quantity: $\mathbb{E}_t[p^k(z,t)] = \langle z|^{\otimes k} C^{(k)} |\Psi_0\rangle\langle\Psi_0|^{\otimes k} |z\rangle^{\otimes k}$. In this case, the terms in (i) are the dominant contributions and we are able to bound the magnitude of the energy-conservation terms in (ii).

We explicitly state our identity for k=2.

Lemma (Second Hamiltonian twirling identity). If a Hamiltonian H satisfies the second no-resonance condition, the following identity holds:

$$C^{(2)}\left[\rho^{(2)}\right] \equiv \mathbb{E}_{t}\left[U_{t}^{\otimes 2}\rho^{(2)}U_{-t}^{\otimes 2}\right]$$

$$= \sum_{E,E'}\left[|E,E'\rangle\langle E,E'|\rho^{(2)}|E,E'\rangle\langle E,E'| + |E,E'\rangle\langle E,E'|\rho^{(2)}|E',E\rangle\langle E',E|\right] - \sum_{E}|E,E\rangle\langle E,E|\rho^{(2)}|E,E\rangle\langle E,E|$$

$$= \mathcal{D}^{\otimes 2}\left[\rho^{(2)}\right]\mathbb{I} + \mathcal{D}^{\otimes 2}\left[\rho^{(2)}\mathcal{S}\right]\mathcal{S} - \sum_{E}|E,E\rangle\langle E,E|\rho^{(2)}|E,E\rangle\langle E,E|,$$
(S2)

where $U_t \equiv \exp(-iHt)$, $\mathbb{E}_t[f(t)] = \lim_{T \to \infty} \frac{1}{T} \int_0^T f(t) dt$ is the average of f(t) over infinite time. $\rho^{(2)}$ is any state on two copies of the Hilbert space, and $|E\rangle$ are energy eigenstates of the Hamiltonian. \mathbb{I} and \mathcal{S} are the identity and swap operators on $\mathcal{H}^{\otimes 2}$, defined as $\mathbb{I}(|\psi_1\rangle \otimes |\psi_2\rangle) = |\psi_1\rangle \otimes |\psi_2\rangle$ and $\mathcal{S}(|\psi_1\rangle \otimes |\psi_2\rangle) = |\psi_2\rangle \otimes |\psi_1\rangle$ for any $|\psi_1\rangle$, $|\psi_2\rangle$. Lastly, $\mathcal{D}^{\otimes 2}$ is the dephasing channel in the energy eigenbasis: $\mathcal{D}^{\otimes 2}[\rho^{(2)}] \equiv \sum_{E,E'} |E,E'\rangle\langle E,E'| \rho^{(2)}|E,E'\rangle\langle E,E'|$. Finally, we remark that the state $\rho^{(2)}$ on $\mathcal{H}^{\otimes 2}$ can be generalized to any operator A acting on $\mathcal{H}^{\otimes 2}$.

Proof.

$$\mathbb{E}_{t}\left[U_{t}^{\otimes 2}\rho^{(2)}U_{-t}^{\otimes 2}\right] = \lim_{T \to \infty} \frac{1}{T} \int_{0}^{T} dt \ U_{t}^{\otimes 2}\rho^{(2)}U_{-t}^{\otimes 2} \tag{S3}$$

$$= \sum_{E_1, E_2, E_3, E_4} \left[\lim_{T \to \infty} \frac{1}{T} \int_0^T dt \ e^{-i(E_1 - E_2 + E_3 - E_4)t} \right] |E_1, E_3| \langle E_1, E_3| \rho^{(2)} |E_2, E_4| \langle E_2, E_4| \rangle$$
(S4)

$$= \sum_{E_1, E_2, E_3, E_4} \delta(E_1 - E_2 + E_3 - E_4) |E_1, E_3| \langle E_1, E_3 | \rho^{(2)} | E_2, E_4 \rangle \langle E_2, E_4 |$$
(S5)

$$\stackrel{\text{2-NR}}{=} \sum_{E,E'} \left[|E,E'\rangle\langle E,E'| \, \rho^{(2)} \, |E,E'\rangle\langle E,E'| + |E,E'\rangle\langle E,E'| \, \rho^{(2)} \, |E',E\rangle\langle E',E| \, \right] - \sum_{E} |E,E\rangle\langle E,E| \, \rho^{(2)} \, |E,E\rangle\langle E,E| \, , \tag{S6}$$

where "(2-NR)" indicates the use of the second no-resonance condition. The second no-resonance condition states that the delta function $\delta(E_1 - E_2 + E_3 - E_4)$ is non-zero in only two cases: $E_1 = E_2$, $E_3 = E_4$ or $E_1 = E_4$, $E_3 = E_2$, which give the two terms above. The final, energy-conservation term in Eq. (S6) corresponds to $E_1 = E_2 = E_3 = E_4$. This special case belongs to the above two terms simultaneously and is double counted. Therefore, the energy-conservation term is subtracted to correct for this double counting.

A diagrammatic representation of this Lemma is shown in Fig. S1(a,b). The energy-conservation terms are illustrated in Fig. S1(c). As with the second Hamiltonian twirling identity, one can define the k-th twirling identity.

Lemma 1 (k-th Hamiltonian twirling identity). If the Hamiltonian satisfies the k-th no-resonance condition, its k-th twirling channel is:

$$C^{(k)}[\rho^{(k)}] \equiv \mathbb{E}_{t} \left[U_{t}^{\otimes k} \rho^{(k)} U_{-t}^{\otimes k} \right]$$

$$= \sum_{M=(E_{1},\cdots,E_{k})} \left[\sum_{\sigma \in \pi(M)} |E_{1},\cdots,E_{k}\rangle\langle E_{1},\cdots,E_{k}| \rho^{(k)} |E_{\sigma(1)},\cdots,E_{\sigma(k)}\rangle\langle E_{\sigma(1)},\cdots,E_{\sigma(k)}| \right], \quad (S7)$$

$$= \mathcal{D}^{\otimes k} \left[\rho^{(k)} \hat{\sigma}^{-1} \right] \sum_{\sigma \in \mathcal{S}} \hat{\sigma} + \text{E.C.} \quad (S8)$$

where $\mathbb{E}_t[f(t)] = \lim_{T \to \infty} \frac{1}{T} \int_0^T f(t)dt$ is averaging over infinite time, $\rho^{(k)}$ is any state on k copies of the Hilbert space $\mathcal{H}^{\otimes k}$, and $\hat{\sigma}$ —with $\sigma \in S_k$ —is a permutation operator acting on the k-copy Hilbert space:

$$\hat{\sigma} = \sum_{\{E_i\}} |E_1, E_2, \dots, E_k \rangle \langle E_{\sigma(1)}, E_{\sigma(2)}, \dots, E_{\sigma(k)}|.$$
(S9)

In (S7), the sum is taken over all possible lists of k energies $M=(E_1,\cdots,E_k)$. If M has r unique energies with multiplicities n_1,\cdots,n_r (such that $\sum_{i=1}^n n_r=k$), its group of permutations $\pi(M)$ has $k!/\prod_{i=1}^n n_i!$ elements and is a subgroup of the symmetric group S_k . In (S8), this identity is re-written in terms of permutations, the dephasing channel $\mathcal{D}^{\otimes k}\left[\rho^{(k)}\right] \equiv \sum_{E_1,\cdots,E_k}|E_1,\cdots,E_k\rangle\langle E_1,\cdots,E_k|$ $\rho^{(k)}|E_1,\cdots,E_k\rangle\langle E_1,\cdots,E_k|$, and energy-conservation terms E.C. associated with double, or multiple, counting (similar to the k=2 case). All terms can be explicitly derived from (S7).

Figure S1. Second and third Hamiltonian twirling identities. (a) The second Hamiltonian twirling identity comprises identity and swap permutations terms, along with an energy-conservation correction term that in our context will have an exponentially small contribution. (b) The same as (a), but open legs representing the channel input/outputs are rearranged in order to simplify the diagram. We keep this convention for the rest of diagrams in this document. (c) Diagrammatic notation for the basic building block in our diagrams: the dephasing operator in the energy eigenbasis: $D[\rho] = \sum_{E} |E\rangle\langle E| \rho |E\rangle\langle E|$. (d) The third Hamiltonian twirling identity comprises of six permutation and several energy-conservation terms. For our purposes, these additional terms will have small contributions.

The proof of the k-th twirling identity is analogous to that of the second twirling identity: in this case, there are k! permutations relevant for the k-th no resonance theorem, along with more energy-conservation terms than the simplest one in the k=2 case. As an example, the third twirling identity is illustrated diagrammatically in Fig. S1(d). In addition to the energy-conservation terms associated with cases where two energies are the same $E_i = E_j$, there is a higher order energy-conservation term when all three energies are the same: $E_1 = E_2 = E_3$.

Lastly, we note that this identity also holds in Floquet systems, as long the k-th no resonance condition is tightened to $\sum_i E_{\alpha_i} \equiv \sum_i E_{\beta_i} \pmod{2\pi} \iff \{\alpha_i\} = \{\beta_i\}$, and the integral over all time is replaced by a discrete sum over integer Floquet periods nT.

D. Porter-Thomas distribution over time

We will use the k-th Hamiltonian twirling identity, with $\rho^{\otimes k} = |\Psi_0\rangle\langle\Psi_0|^{\otimes k}$, to prove that the quantity $\tilde{p}(z,t) \equiv p(z,t)/p_{\text{avg}}(z)$ asymptotically follows the *Porter-Thomas*, or exponential distribution [7].

The Porter-Thomas (PT) distribution naturally arises from the distribution of overlaps p of the Haar ensemble — the unique distribution of states on the Hilbert space that is invariant under any unitary — to a fixed vector $|\Phi\rangle$: $p = |\langle \Psi | \Phi \rangle|^2$, with $|\Psi\rangle$ drawn from the Haar ensemble. A given $|\Psi\rangle$ and $|\Phi\rangle$ have overlap $|\langle \Psi | \Phi \rangle|^2$. The probability density of obtaining an overlap with value p is $P(p) = \int d\Psi \delta(|\langle \Psi | \Phi \rangle|^2 = p)$. In deep random circuits, the wavefunction $|\Psi\rangle$ is approximately Haar-random and we can evaluate P(p) for any Hilbert space dimension D, which converges to the Porter-Thomas distribution in the limit $D \to \infty$.

$$P(p)dp = (D-1)(1-p)^{D-2}dp \xrightarrow{D\to\infty} \exp(-Dp)d(Dp) , \qquad (S10)$$

It is natural to rescale the quantity p by D. In this case, the exponential distribution has a k-th moment $\int_0^\infty (Dp)^k P(Dp) d(Dp) = k!$.

We formally state the Theorem from the main text in Theorems 1 and 2 below. Informally, our theorems show that the normalized distribution $\tilde{p}(z,t) \equiv p(z,t)/p_{\rm avg}(z)$ asymptotically follows the PT distribution. As a reminder, $p(z,t) = |\langle z|\Psi(t)\rangle|^2$ is the probability of measuring outcome z, and $p_{\rm avg}(z) = \mathbb{E}_t\left[p(z,t)\right]$ is its time-averaged value.

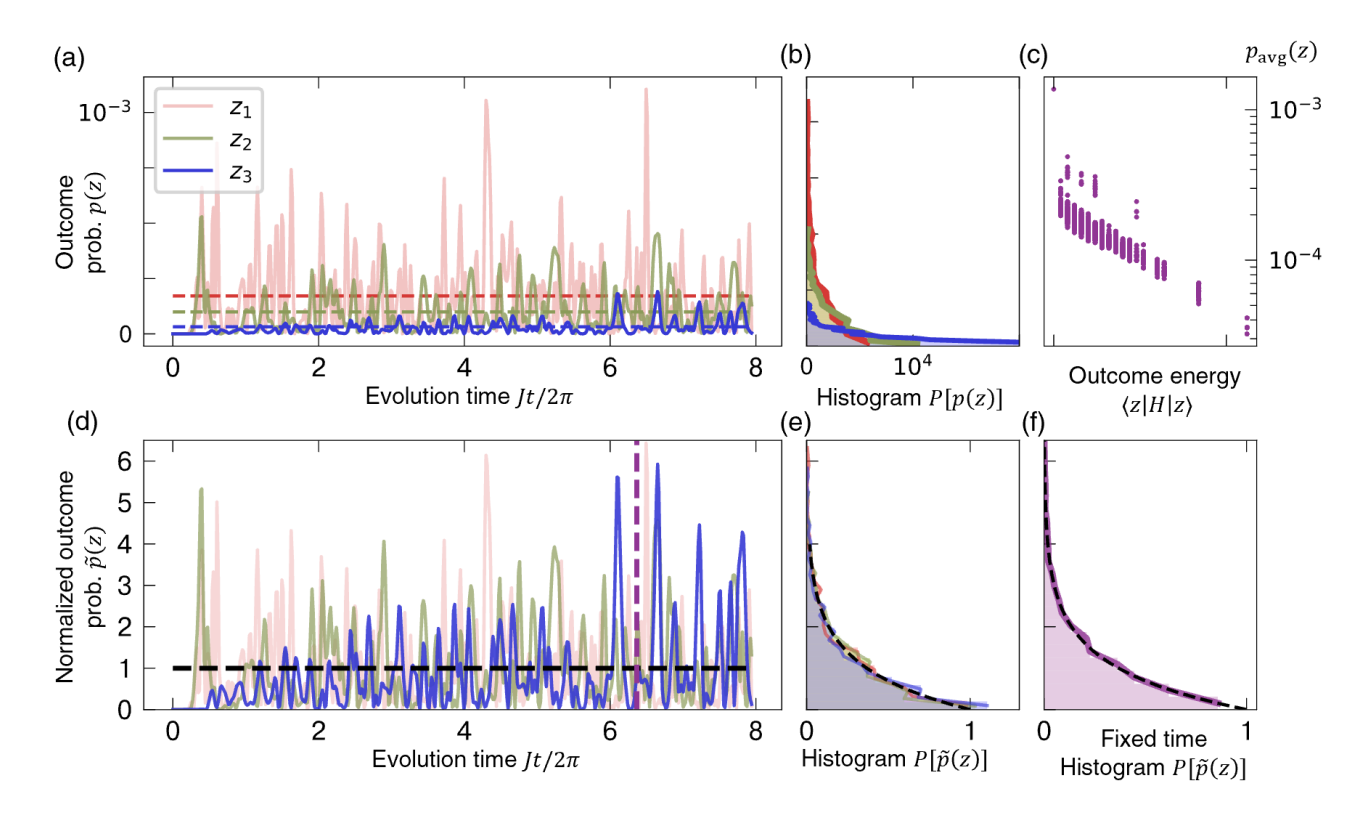


Figure S2. (a) Outcome probabilities p(z,t) over time, for three outcomes z_1, z_2, z_3 in a Bose-Hubbard model with 8 particles on 8 sites in red, green and blue respectively. For each z, p(z,t) fluctuates about its mean value $p_{\text{avg}}(z)$ (dashed lines). (b) Plotting the histogram of p(z,t) over time, each histogram follows an exponential distribution with differing means $p_{\text{avg}}(z)$. (c) $p_{\text{avg}}(z)$ is approximately exponentially dependent on the outcome energy $\langle z|H|z\rangle$, analogous to a Boltzmann distribution. (d) The normalized outcome probabilities $\tilde{p}(z,t)$ follow (e) a universal exponential (Porter Thomas) distribution, which follows from Theorem 1. (f) Taking a histogram at fixed time [purple, (d)] over bitstrings z gives the same distribution (Theorem 2).

By showing that the k-th moments of $\tilde{p}(z,t)$ are close to k!, we show that $\tilde{p}(z,t)$ asymptotically approaches the Porter-Thomas distribution. We can choose to fix the bitstring z, and consider the ensemble over times t [Theorem 1, Fig. S2(d,e)], or fix a large but arbitrary time t, and consider the ensemble of $\tilde{p}(z,t)$ over outcomes z [Theorem 2, Fig. S2(d,f)]. For brevity, we will occasionally denote these ensembles as $\{\tilde{p}(z,t)\}_t$ and $\{\tilde{p}(z,t)\}_z$ respectively, with the subscript denoting the variable over which the ensemble is formed (the other variable is kept fixed). Formally stated, our first Theorem is the following:

Theorem 1 (Temporal Porter-Thomas distribution). For an initial state $|\Psi_0\rangle$ and a Hamiltonian H satisfying the k-th no-resonance condition, the temporal k-th moment of $\tilde{p}(z,t)$ (with fixed z), approaches a universal value $\mathbb{E}_t \left[\tilde{p}(z,t)^k \right] = k! + O(D_{\beta}^{-1}(z))$. $D_{\beta}(z)$ is the effective Hilbert space dimension of the outcome z defined as $D_{\beta}^{-1}(z) \equiv \left(\sum_E |\langle z|E \rangle|^4 |\langle E|\Psi_0 \rangle|^4 \right) / p_{avg}(z)^2$.

Proof. Our proof is a direct application of our k-th Hamiltonian twirling identity on the temporal k-th moment $\mathbb{E}_t\left[\tilde{p}(z,t)^k\right]=k!+O(D_\beta^{-1})$: To compute $\mathbb{E}_t\left[\tilde{p}(z,t)^k\right]$, we apply Lemma 1 on $\rho^{(k)}=|\Psi_0\rangle\langle\Psi_0|^{\otimes k}$:

$$\mathbb{E}_{t}\left[\tilde{p}(z,t)^{k}\right] = \frac{\langle z|^{\otimes k} \,\mathbb{E}_{t}\left[U_{t}^{\otimes k} \,|\Psi_{0}\rangle\langle\Psi_{0}|^{\otimes k} \,U_{-t}^{\otimes k}\right] |z\rangle^{\otimes k}}{p_{\text{avg}}(z)^{k}} \tag{S11}$$

$$=\frac{\sum_{M=(E_1,\cdots,E_k)}\sum_{\sigma\in\pi(M)}\left[\prod_{i=1}^k\left|\langle z|E_i\rangle\left\langle E_{\sigma_i}|\Psi_0\rangle\right|^2\right]}{p_{\text{avg}}(z)^k}=\frac{\sum_{M=(E_1,\cdots,E_k)}\left|\pi(M)\right|\left[\prod_{i=1}^k\left|\langle z|E_i\rangle\left\langle E_i|\Psi_0\rangle\right|^2\right]}{p_{\text{avg}}(z)^k}$$
(S12)

where we have used Eq. (S7). Now using Eq. (S8), where the contribution from the first term is equivalent to replacing $|\pi(M)|$ with k!. This gives:

$$\frac{\langle z|^{\otimes k} \mathcal{D}^{\otimes k} \left[|\Psi_0\rangle \langle \Psi_0|^{\otimes k} \right] \left[\sum_{\sigma \in S_k} \hat{\sigma} \right] |z\rangle^{\otimes k}}{p_{\text{avg}}(z)^k} = k! \frac{\sum_{\{E_j\}} \prod_{j=1}^k |\langle z|E_j\rangle \langle E_j|\Psi_0\rangle|^2}{p_{\text{avg}}(z)^k} = k! ,$$
 (S13)

where in the first equality we used the fact that $\hat{\sigma}$ operator acts trivially on the product state $|z\rangle^{\otimes k}$ and in the second equality, we used the relation

$$p_{\text{avg}}(z) \equiv \mathbb{E}_t \left[p(z, t) \right] = \sum_E \left| \langle z | E \rangle \langle E | \Psi_0 \rangle \right|^2 .$$
 (S14)

This relation is used several times, motivating our definition of the quantity

$$q_z(E) \equiv \frac{\left| \langle z|E\rangle\langle E|\Psi_0\rangle \right|^2}{p_{\text{avg}}(z)} \tag{S15}$$

In fact, $q_z(E)$ has the properties of a probability distribution over the energies E: $0 \le q_z(E) \le 1$ and $\sum_E q_z(E) = 1$. Now we wish to bound the deviation $|\mathbb{E}_t\left[\tilde{p}(z,t)^k\right] - k!|$, that is the contribution from all energy-conservation (E.C.) terms. To do so, we note the E.C. terms must come from lists of energies $M = (E_1, \dots, E_k)$ with at least one repeated energy. That is:

$$\left| \mathbb{E}_{t} \left[\tilde{p}(z, t)^{k} \right] - k! \right| \equiv \left| \frac{\langle z |^{\otimes k} \left(\text{E.C.} \right) | z \rangle^{\otimes k}}{p_{\text{avg}}(z)^{k}} \right| = \sum_{\substack{M = (E_{1}, \dots, E_{k}) \\ \text{not all } E_{j} \text{ distinct}}} |\pi(M) - k! | \prod_{j=1}^{k} q_{z}(E_{j})$$
(S16)

$$\leq k! \left[\sum_{E_1 = E_2} \sum_{E_3, \dots, E_k} \prod_{j=1}^k q_z(E_j) + \sum_{E_1 = E_3} \sum_{E_2, E_4, \dots, E_k} \prod_{j=1}^k q_z(E_j) + \dots \right]$$

In the last line, we have used two separate inequalities: we bound the difference $|\pi(M) - k!| \le k!$. This enables us to contain all possible lists M with at least one repeated energy in the sums above, where we have only explicitly demanded that one pair of energies coincide: $E_a = E_b$. There are $\binom{k}{2}$ choices of a and b. Each choice has the same value. Therefore without loss of generality, we set a = 1 and b = 2. Then we obtain:

$$\left| \mathbb{E}_t \left[\tilde{p}(z,t)^k \right] - k! \right| \le k! \binom{k}{2} \sum_{E_1} q_z(E_1)^2 \prod_{j=3}^k \sum_{E_j} q_z(E_j) = k! \binom{k}{2} \sum_{E_1} q_z(E_1)^2 \equiv k! \binom{k}{2} D_{\beta}^{-1}(z) . \tag{S17}$$

Therefore, we obtain the desired bound

$$\left| \mathbb{E}_t \left[\tilde{p}(z,t)^k \right] - k! \right| \le k! \binom{k}{2} D_{\beta}^{-1}(z) = O(D_{\beta}^{-1}(z))$$
 (S18)

In fact, we expect this bound to be close to tight: the contribution from the simplest energy-conservation terms — those with exactly one repeated energy — is close to our bound. Other energy-conservation terms are expected to be exponentially smaller than these simplest terms. Here, the factor $\pi(M) = k!/2$, and we obtain:

$$\mathbb{E}_t\left[\tilde{p}(z,t)^k\right] \approx k! \left(1 - \frac{k(k-1)}{2} \frac{D_{\beta}^{-1}(z)}{2}\right) . \tag{S19}$$

Eq. (S19) agrees with the leading order (in D^{-1}) correction to the k-th moment of the Porter-Thomas distribution:

$$\int_0^1 dp \ p^k (D-1)(1-p)^{D-2} = k! \frac{D^k}{D \cdots (D+k-1)} = k! \left[1 - \frac{k(k-1)}{2} D^{-1} + O(D^{-2}) \right] . \tag{S20}$$

Therefore, it is apt to call $D_{\beta}(z)$ as the effective dimension: the deviation of the k-th moment from k! for the temporal distribution is the same as that of the Porter-Thomas distribution for a system with finite dimension $2D_{\beta}$. $\{\tilde{p}(z,t)\}_t$ approximately follows a Porter-Thomas distribution over a vector space of dimension $2D_{\beta}(z)$. Note, however, that this agreement does not extend to corrections of higher orders in D^{-1} .

For a fixed z, the inverse effective dimension $D_{\beta}^{-1}(z)$ can be understood as the *collision probability* associated with $q_z(E)$. More explicitly, we can define $D_{\beta}^{-1}(z) = \sum_E q_z(E)^2$ such that $D_{\beta}(z)$ describes the participation ratio (or equivalently the size of effective Hilbert space dimension) corresponding to a particular bitstring z. Then the overall inverse participation ratio (inverse effective dimension) D_{β}^{-1} is the weighted average: $D_{\beta}^{-1} = \sum_z p_{\text{avg}}(z) D_{\beta}^{-1}(z)$.

E. Porter-Thomas distribution over outcomes

Theorem 2 concerns the distribution of $\tilde{p}(z,t)$ for fixed t, treated as samples labeled by z.

Theorem 2 (Porter-Thomas distribution over outcomes). Consider an initial state $|\Psi_0\rangle$ and a Hamiltonian H satisfying the 2k-th no-resonance condition. At a typical time $t \in [0, \infty)$, the weighted k-th moment of $\tilde{p}(z, t)$ approaches a universal value: $P^{(k)}(t) \equiv \sum_z p_{avg}(z)\tilde{p}(z, t)^k = k! + O(D_{\beta}^{-1/2})$, where $D_{\beta}^{-1} \equiv \sum_{z,E} |\langle z|E\rangle|^4 |\langle E|\Psi_0\rangle|^4 / p_{avg}(z)$ is the inverse effective Hilbert space dimension associated with the quench evolution, and $\{|E\rangle\}$ are the eigenstates of H.

Proof. Our proof strategy is the following. We first compute the time-averaged value $\mathbb{E}_t\left[P^{(k)}(t)\right]$. From Theorem I, this quantity is $k! + O(D_{\beta}^{-1})$. We next compute the fluctuations of $P^{(k)}(t)$ over time, and we will find that $\operatorname{std}_t\left[P^{(k)}(t)\right] = O(D_{\beta}^{-1/2})$. Combining these two results leads to our desired conclusion: $P^{(k)}(t) = k! + O(D_{\beta}^{-1/2})$ with high probability.

In Fig. S3(a), we illustrate this computation of $\mathbb{E}_t \left[P^{(k)}(t) \right]$ for the case k=2. In general, we have:

$$\left| \mathbb{E}_t \left[P^{(k)}(t) \right] - k! \right| \le \sum_z p_{\text{avg}}(z) \left| \mathbb{E}_t \left[\tilde{p}(z, t)^k \right] - k! \right| \le \binom{k}{2} k! \sum_z p_{\text{avg}}(z) D_{\beta}^{-1}(z) = O(D_{\beta}^{-1})$$
 (S21)

Up to this point, we have only used the k-th Hamiltonian twirling identity. To estimate the temporal fluctuations of $P^{(k)}(t)$, we need the 2k-th twirling identity.

$$\operatorname{var}_{t}[P^{(k)}(t)] = \mathbb{E}_{t}[P^{(k)}(t)^{2}] - \mathbb{E}_{t}[P^{(k)}(t)]^{2} = \sum_{z,z'} p_{\operatorname{avg}}(z) p_{\operatorname{avg}}(z') \frac{\mathbb{E}_{t}[p(z,t)^{k}p(z',t)^{k}] - \mathbb{E}_{t}[p(z,t)^{k}]\mathbb{E}_{t}[p(z',t)^{k}]}{p_{\operatorname{avg}}(z)^{k} p_{\operatorname{avg}}(z')^{k}}$$
(S22)

By using the Hamiltonian k-th and 2k-th twirling identities, any term in $\mathbb{E}_t[P^{(k)}(t)^2]$ that does not cancel with a term in $\mathbb{E}_t[P^{(k)}(t)]^2$ must involve a permutation between z and z' [illustrated for k=2 in Fig. S3(b)]. As in our proof of Theorem 1, without loss of generality, we let the energies corresponding to this permutation be E_1 and E_2 , and multiply our overall expression by a factor of $2\binom{2k}{2}$ (here, E_1 and E_2 are inequivalent). Then their sum is of the form

$$\operatorname{var}_{t}[P^{(k)}(t)] = \sum_{z,z'} p_{\operatorname{avg}}(z) p_{\operatorname{avg}}(z') 2 \binom{2k}{2} \frac{\sum_{E_{1},E_{2}} \left| \langle E_{1} | \Psi_{0} \rangle \right|^{2} \left\langle z | E_{1} \rangle \langle E_{1} | z' \rangle \left| \langle E_{2} | \Psi_{0} \rangle \right|^{2} \left\langle z' | E_{2} \rangle \langle E_{2} | z \rangle}{p_{\operatorname{avg}}(z) p_{\operatorname{avg}}(z')} (\cdots)$$
 (S23)

$$\equiv \sum_{z,z'} p_{\text{avg}}(z) p_{\text{avg}}(z') 2 \binom{2k}{2} \frac{\langle z | \rho_d | z' \rangle \langle z' | \rho_d | z \rangle}{p_{\text{avg}}(z) p_{\text{avg}}(z')} (\cdots) , \qquad (S24)$$

$$(\cdots) = \sum_{\text{perms.}} \prod_{j=3}^{2k} \frac{\sum_{E_j} \left| \langle E_j | \Psi_0 \rangle \right|^2 \left\langle z_j^L | E_j \rangle \left\langle E_j | z_j^R \right\rangle}{\sqrt{p_{\text{avg}}(z_j^L) p_{\text{avg}}(z_j^R)}} \equiv \sum_{\text{perms.}} \prod_{j=3}^{2k} \frac{\langle z_j^L | \rho_d | z_j^R \rangle}{\sqrt{p_{\text{avg}}(z_j^L) p_{\text{avg}}(z_j^R)}} \le \sum_{\text{perms.}} 1 \le (2k-2)! \quad (S25)$$

where z_j^L and z_j^R can either be z or z', such that there exactly k-1 of the $\{z_j^L\}$ are z and the other k-1 are z', and likewise for the $\{z_j^R\}$. For brevity, we have also rewritten our expressions with $\rho_d \equiv \sum_E |\langle E|\Psi_0\rangle|^2 |E\rangle\langle E|$, the commonly studied diagonal ensemble [2, 8]. Note that $p_{\text{avg}}(z) = \langle z|\rho_d|z\rangle$.

commonly studied diagonal ensemble [2, 8]. Note that $p_{\text{avg}}(z) = \langle z | \rho_d | z \rangle$. The inequalities in (S25) are obtained as follows. The term involving ρ_d is bounded by a simple application of the Cauchy-Schwarz identity, gives $|\langle z | \rho_d | z' \rangle|^2 \leq p_{\text{avg}}(z)p_{\text{avg}}(z')$. Since $|\langle z | \rho_d | z \rangle|^2 \equiv p_{\text{avg}}(z)p_{\text{avg}}(z')$, it follows that $|\langle z_j^L | \rho_d | z_j^R \rangle|/\sqrt{p_{\text{avg}}(z_j^L)p_{\text{avg}}(z_j^R)} \leq 1$ regardless of the values of z_j^L and z_j^R . Finally, the sum $\sum_{\text{perms.}}$ is a sum over allowed permutations of a given list of energies (E_1, \cdots, E_{2k}) ; we bound this by (2k-2)!. (Formally, $\sum_{\text{perms.}}$ should be inside the summation over energies, with different permutations giving rise to different realizations of $\{z_j^L, z_j^R\}$. However, we use the notation above because this sum only gives a constant factor.)

Combining (S24) and (S25), we obtain

$$\operatorname{var}_{t}[P^{(k)}(t)] = (2k)! \sum_{z,z'} p_{\operatorname{avg}}(z) p_{\operatorname{avg}}(z') \frac{\langle z | \rho_{d} | z' \rangle \langle z' | \rho_{d} | z \rangle}{p_{\operatorname{avg}}(z) p_{\operatorname{avg}}(z')} = (2k)! \operatorname{tr}(\rho_{d}^{2}) \le (2k)! D_{\beta}^{-1}$$
 (S26)

In our last inequality, we used $\operatorname{tr}(\rho_d^2) \leq D_{\beta}^{-1}$. This is derived from Sedrakyan's inequality, which states that for positive u_i and v_i , $(\sum_i u_i)^2 / \sum_i v_i \leq \sum_i (u_i^2/v_i)$. In our context,

$$\operatorname{tr}(\rho_d^2) \equiv \sum_{E} |\langle \Psi_0 | E \rangle|^4 = \sum_{E} |\langle \Psi_0 | E \rangle|^4 \frac{\left(\sum_{z} |\langle z | E \rangle|^2\right)^2}{\sum_{z} p_{\text{avg}}(z)} \le \sum_{z, E} \frac{|\langle z | E \rangle \langle E | \Psi_0 \rangle|^4}{p_{\text{avg}}(z)} \equiv D_{\beta}^{-1} . \tag{S27}$$

This completes our proof that for a typical t, $P^{(k)}(t) = k! + O(D_{\beta}^{-1/2})$.

Our theorem states that when D_{β} is sufficiently large, the k-th moment of $\{p(z,t)\}$ is close to k!. We can then conclude that $\{p(z,t)\}$ follows the exponential distribution when D_{β} is sufficiently large. Our numerical results support this: fixing a late enough time t (we numerically find that a time scaling linearly in system size is sufficient for our purposes) and plotting the histogram of the normalized probabilities $\{\tilde{p}(z,t)\}_z$ (weighted by $p_{\text{avg}}(z)$) shows a good agreement with the exponential distribution, as seen in Fig. S2(f).

Theorems 1 and 2 together suggest an analogue to the ergodic theorem in classical dynamical systems. Consider an ensemble of particles in a classical dynamical system, such as a billiard stadium. The ergodic theorem states that the spatial distribution of this ensemble at a fixed time is the same as the distribution of a fixed particle over time. In our context, the distributions of $\tilde{p}(z,t)$ are asymptotically the same in two settings: with fixed t over configurations t and with fixed t over t. Furthermore, both distributions limit to the universal Porter-Thomas distribution.

II. DETAILED PERFORMANCE ANALYSIS FOR LONG QUENCH DYNAMICS

In this section we apply the above results to characterize the accuracy of our fidelity estimator F_d . Our analysis is valid when the state has reached global equilibrium, quantified by the quantity $P^{(2)}(t) \equiv \sum_z p_{\text{avg}}(z) \tilde{p}(z,t)^2$ reaching its equilibrium value of 2. In Theorem 2, we have bounded the deviation of the k-th moments $P^{(k)}(t)$ from its ideal value of k!. Under an approximation [Eq. (S32)], our bound for $P^{(2)}(t)$ is sufficient to claim that the F_d formula approximates F with accuracy that is exponentially good in system size. By keeping the simplest energy-conservation terms that are the leading-order corrections in Theorem 2, we make quantitative predictions for the systematic error δ_{sys} and temporal fluctuations δ_{temp} . We explicitly confirm our theoretical analysis via numerical simulations presented in Fig. 2 of our main text and Fig. S4, which shows excellent agreement between theory prediction and numerical results. This suggests that our formalism presented here is able to capture the performance of the F_d formula to first order in D_{β}^{-1} , at least for the system sizes investigated.

We define the following relevant quantities:

$$F_{\rm id,d}(t) \equiv \sum_{z} p_{\rm avg}(z)\tilde{p}(z,t)^2 - 1 = P^{(2)}(t) - 1$$
, (S28)

$$F_{\text{XEB,d}}(t) \equiv \sum_{z} p_{\text{avg}}(z)\tilde{q}(z,t)\tilde{p}(z,t) - 1 . \qquad (S29)$$

 $F_{\mathrm{id,d}}$ is a measure of whether the state has reached global equilibrium: after equilibration, $F_{\mathrm{id,d}} \approx 1$, while at very short times, $F_{\mathrm{id,d}} \sim O(D)$ is exponentially large when the initial state is a product state or a lowly-entangled state. $F_{\mathrm{XEB,d}}$ is analogous to the linear cross-entropy benchmark F_{XEB} . Our formula F_d can be re-expressed as $F_d = 2(F_{\mathrm{XEB,d}} + 1)/(F_{\mathrm{id,d}} + 1) - 1$.

We can bound $F_{\rm id,d} \geq 0$ and $F_{\rm XEB,d} \geq -1$. This gives:

$$-1 \le F_d \le 2\sqrt{\frac{\sum_z p_{\text{avg}}(z)\tilde{q}(z)^2}{\sum_z p_{\text{avg}}(z)\tilde{p}(z)^2}} - 1 , \qquad (S30)$$

We compute the average values over time of F_d as well as its variance over time. The typical variance is exponentially small in system size, therefore sampling at a single late time will give values close to its mean.

We use "exponentially small in system size" as a shorthand to mean that a quantity is proportional to a measure of the effective dimension: D_{β}^{-1} or $\operatorname{tr}(\rho_d^2)$. These are related by the following inequalities:

$$D^{-1} \le \sum_{z} p_{\text{avg}}(z)^2 \le \text{tr}(\rho_d^2) \le D_\beta^{-1} \le 1$$
 (S31)

The first inequality is a straightfoward inequality between the arithmetic and quadratic means. The second inequality is obtained immediately by noting that $\operatorname{tr}(\rho_d)^2 = \sum_z p_{\operatorname{avg}}(z)^2 + \sum_{z \neq z'} |\langle z| \, \rho_d \, |z' \rangle|^2 \geq \sum_z p_{\operatorname{avg}}(z)^2$, and the final inequality was established in Eq. (S27). D_β^{-1} is in general only upper bounded by 1, since choosing $|z\rangle = |E\rangle = |\Psi_0\rangle$, gives $D_\beta^{-1} = 1$. However, for generic initial states, we expect D_β^{-1} to be exponentially small in system size.

A. Ansatz for how speckle patterns change under errors

In the long-time limit, it is fruitful to approximate $\tilde{q}(z)$ as:

$$\tilde{q}(z) \approx F\tilde{p}(z) + (1 - F)\tilde{p}_{\perp}(z)$$
, (S32)

for some uncorrelated distribution $\tilde{p}_{\perp}(z)$. We do not require $\tilde{p}_{\perp}(z)$ to also follow Porter-Thomas statistics. Indeed, $\tilde{p}_{\perp}(z)$ does not generally follow a PT distribution in the case of incoherent errors.

We further assume that $\tilde{p}(z)$ and $\tilde{p}_{\perp}(z)$ are uncorrelated. This allows us to make the following approximation, which will arise in several places:

$$\sum_{z} p_{\text{avg}}(z) \tilde{p}_{\perp}(z) \tilde{p}(z)^{k} \approx \sum_{z} p_{\text{avg}}(z) \tilde{p}_{\perp}(z) \sum_{z'} p_{\text{avg}}(z') \tilde{p}(z')^{k} \approx k! , \qquad (S33)$$

where we have used that $\sum_{z} p_{\text{avg}}(z) \tilde{p}_{\perp}(z) = 1$ since $p_{\text{avg}}(z) \tilde{p}_{\perp}(z) = p_{\perp}(z)$. This illustrates that we do not require $\tilde{p}_{\perp}(z)$ to follow the Porter-Thomas distribution — the energy density of the perturbed state can be quite different from the target state, as is the case when many errors occur. As an example, applying this on Eq. (S29) gives the desired $F_{\text{XEB,d}} \approx F$.

A related approximation applicable to higher order correction terms, is to assume a coherent error V, and write the experimental state as $|\psi'(t)\rangle = V(t) |\psi_0(t)\rangle$. V(t) is unitary, and therefore $V^{\dagger}(t)V(t) = \mathbb{I}$. However, we replace instances of V(t) or $V^{\dagger}(t)$ that do not cancel with their Hermitian conjugates with

$$V(t), V^{\dagger}(t) \to \sqrt{F}$$
 (S34)

While crude, this approximation is useful to make quick estimates. Furthermore, its predictions quantitatively agree with our numerical results, indicating that the dominant sources of error are due to the structure of the F_d formula, which we discuss below.

B. Systematic error

Here, we characterize the systematic error $\delta_{\text{sys.}} \equiv \mathbb{E}_t \left[F_d(t) \right] - F$: the difference between the time-averaged F_d and the true fidelity F after an isolated error. To do so, we first study the time average of the simpler quantities $F_{\text{id,d}}(t) \equiv \sum_z p_{\text{avg}}(z) \tilde{p}(z,t)^2 - 1$ and $F_{\text{XEB,d}}(t) \equiv \sum_z p_{\text{avg}}(z) \tilde{p}(z,t) \tilde{q}(z,t) - 1$.

The k-th moment of the PT distribution (Theorems 1,2) immediately allows us to estimate $F_{id,d}$:

$$\mathbb{E}_{t}\left[F_{\text{id,d}}(t)\right] = \mathbb{E}_{t}\left[\sum_{z} p_{\text{avg}}(z)\tilde{p}^{2}(z,t) - 1\right] = 1 - D_{\beta}^{-1} . \tag{S35}$$

Using (S34) gives

$$F_{\rm XEB,d} \approx F(1 - D_{\beta}^{-1}) . \tag{S36}$$

We would like to use these results to obtain the time-averaged value of F_d . The time average of the numerators and denominators $F_{\text{XEB,d}}$ and $F_{\text{id,d}}$ should be done together. We can estimate its effects with the following Taylor expansion:

$$\mathbb{E}\left[\frac{X}{Y}\right] \approx \frac{\mathbb{E}[X]}{\mathbb{E}[Y]} - \frac{\text{cov}[X,Y]}{\mathbb{E}[Y]^2} + \frac{\text{var}[Y]\mathbb{E}[X]}{\mathbb{E}[Y]^3} , \tag{S37}$$

which gives the estimate for the systematic error in the presence of a single error:

$$\delta_{\text{sys}} = \mathbb{E}_t \left[F_d \right] - F \approx (1 - F) \left[\frac{D_{\beta}^{-1}}{2} + \frac{\text{var}_t \left[F_{\text{id,d}} \right]}{8} \right] . \tag{S38}$$

This prediction agrees well with numerical simulations in Fig. S4(a) and Fig. 2b in the main text.

1. Argument based on Eigenstate Thermalization Hypothesis

In the limit of low error rates and long-time evolution, we can show that $F_d \approx F$, independent of our approximation for \tilde{q} (S32). To do so, we consider the effect of a single error V that occurs at a variable time t. In the limit of long evolution, $F_d \approx F_{\text{XEB,d}} \equiv \sum_z p_{\text{avg}}(z) \tilde{q}(z) \tilde{p}(z) - 1$ since the denominator in F_d approaches 2. Therefore, we will show that $F_{\text{XEB,d}} \approx F$ for a single error averaged over the error occurrence time. In the presence of multiple errors, the above relation will hold, as long as the errors are sufficiently far apart in time. We average over two quantities: (i) the time t at which the error V occurs, and (ii) the time τ after the error happens when the measurement is made. At this time, the ideal state is $|\Psi(t+\tau)\rangle$, while the perturbed state is $V(\tau) |\Psi(t+\tau)\rangle$, with $V(\tau) \equiv \exp(-iH\tau)V \exp(iH\tau)$ the Heisenberg evolution of V. Here, the fidelity $F(t) = |\langle \Psi(t+\tau)|V(\tau)|\Psi(t+\tau)\rangle|^2 = |\langle \Psi(t)|V|\Psi(t)\rangle|^2$ is independent of τ and only depends on t (the time when the error is applied), while the XEB depends on both t and τ . We will average both t and τ . We first average over t to compute the average value of $F_{\text{XEB,d}}$ at a time τ after an error is applied:

$$\mathbb{E}_{t}\left[F_{\text{XEB,d}}(t,\tau)\right] = \sum_{z} \frac{\left|\left\langle z\right|V(\tau)\rho_{d}\left|z\right\rangle\right|^{2}}{p_{\text{avg}}(z)} - \sum_{z} \frac{\left\langle z,z\right|\left(V^{\dagger}(\tau)\otimes\mathbb{I}\right)\rho_{d}^{(2)}\left(V(\tau)\otimes\mathbb{I}\right)\left|z,z\right\rangle}{p_{\text{avg}}(z)},$$
(S39)

where we have defined the diagonal ensemble ρ_d and its analog $\rho_d^{(2)}$ over $\mathcal{H}^{\otimes 2}$ as follows:

$$\rho_d \equiv \sum_{E} |\langle E|\Psi_0\rangle|^2 |E\rangle\langle E| = \mathbb{E}_t [|\Psi(t)\rangle\langle\Psi(t)|]$$
 (S40)

$$\rho_d^{(2)} \equiv \sum_E |\langle E|\Psi_0\rangle|^4 |E, E\rangle\langle E, E| \tag{S41}$$

 $\rho_d^{(2)}$ is an analog of ρ_d defined over two-copies of the Hilbert space. The first term in Eq. (S39) is the dominant contribution, while the second term comes from the energy-conservation term in Eq. (S2).

We next average over the time τ after the error, in order to claim that $\mathbb{E}_t \left[F_{\text{XEB,d}}(t,\tau) \right] \approx \mathbb{E}_t \left[F(t) \right]$. The averaging over τ gives:

$$\mathbb{E}_{\tau}\mathbb{E}_{t}\left[F_{\text{XEB,d}}(t,\tau)\right] = \sum_{z} \frac{\langle z|\,\rho_{d}V_{d}\,|z\rangle\langle z|\,\rho_{d}V_{d}^{\dagger}\,|z\rangle}{p_{\text{avg}}(z)} - \sum_{z} \frac{\langle z,z|\,\rho_{d}^{(2)}\left(V_{d}\otimes V_{d}^{\dagger}\right)|z,z\rangle}{p_{\text{avg}}(z)} , \tag{S42}$$

where $V_d \equiv \sum_E |E\rangle\langle E| \ V \ |E\rangle\langle E|$ is the error operator dephased in the energy basis, or the time-averaged operator $\mathbb{E}_{\tau}V(\tau)$. We interpret the first term — the dominant contribution to (S48) — as the average fidelity of states $|\tilde{z}\rangle \propto \sqrt{\rho_d} |z\rangle$ after the error operator V_d :

$$\sum_{z} \frac{\langle z | \rho_{d} V_{d} | z \rangle \langle z | \rho_{d} V_{d}^{\dagger} | z \rangle}{p_{\text{avg}}(z)} = \sum_{z} \frac{\langle z | \sqrt{\rho_{d}} V_{d} \sqrt{\rho_{d}} | z \rangle \langle z | \sqrt{\rho_{d}} V_{d}^{\dagger} \sqrt{\rho_{d}} | z \rangle}{p_{\text{avg}}(z)} = \sum_{z} p_{\text{avg}}(z) |\langle \tilde{z} | V_{d} | \tilde{z} \rangle|^{2} , \qquad (S43)$$

 $|\tilde{z}\rangle \equiv \sqrt{\rho_d}\,|z\rangle\,/\sqrt{p_{\rm avg}(z)}$ is a normalized wavefunction, after a transformation of a computational basis state. We interpret this transformation as an imaginary time evolution generated by the modular Hamiltonian of ρ . We now interpret F_d as an average fidelity $|\langle \tilde{z}|V_d\,|\tilde{z}\rangle|^2$ of an error operator V_d is applied to $|\tilde{z}\rangle$.

We want to relate $\mathbb{E}_{\tau}\mathbb{E}_{t}\left[F_{\text{XEB,d}}(t,\tau)\right]$ to the fidelity $\mathbb{E}_{t}\left[F(t)\right]$ averaged over the time t that the error occurred. This is given by:

$$\mathbb{E}_{t}\left[F(t)\right] = \mathbb{E}_{t}\left[\left|\left\langle\Psi(t)\right|V\left|\Psi(t)\right\rangle\right|^{2}\right] = \left|\operatorname{tr}(\rho_{d}V)\right|^{2} + \operatorname{tr}\left(\rho_{d}V\rho_{d}V^{\dagger}\right) - \operatorname{tr}\left[\rho_{d}^{(2)}(V\otimes V^{\dagger})\right], \tag{S44}$$

with the terms ordered by (expected) magnitude.

In order to relate Eq. (S39) and (S44), we make two observations: (i) for a product initial state $|\Psi_0\rangle$ and local Hamiltonian H, ρ_d approaches a microcanonical state since its energy variance vanishes relative to the size of the spectrum. This is because H is local, implying that $\operatorname{tr}(H^2) \propto N^2$. Therefore, the eigenvalues of H are spread over an energies scaling with total system size N. Meanwhile, (ii) by the locality of H the uncertainty in energy of a product state is of order \sqrt{N} : $\Delta E^2 \equiv \langle \Psi_0 | H^2 | \Psi_0 \rangle - \langle \Psi_0 | H | \Psi_0 \rangle^2 \propto N$. We model the distribution of energies as a Gaussian distribution with mean $\bar{E} \equiv \langle \Psi_0 | H | \Psi_0 \rangle$ and variance ΔE^2 :

$$\sum_{E=\bar{E}-dE/2}^{\bar{E}+dE/2} \left| \langle E|\Psi_0 \rangle \right|^2 \approx \rho \left(\bar{E}\right) \overline{\left| \langle E|\Psi_0 \rangle \right|^2} dE \approx \frac{1}{\Delta E \sqrt{2\pi}} \exp\left(-\frac{(E-\bar{E})^2}{2(\Delta E)^2} \right) dE , \tag{S45}$$

where $\rho(\bar{E})$ is the density of states around \bar{E} . We define this such that $\int \rho(E)dE = D$, such that $\rho(\bar{E}) = \exp(cN)$ for some c > 0. Eq. (S45) also gives the estimate $\sum_{E=\bar{E}-dE/2}^{\bar{E}+dE/2} |\langle E|\Psi_0\rangle|^4 \propto 1/[\rho(\bar{E})\Delta E] \sim \exp(-cN)$ (omitting polynomial factors of N).

(iii) Lastly, the Eigenstate Thermalization Hypothesis (ETH) states that the diagonal elements $\langle E|V|E\rangle$ of a local operator V are well described by a smooth function of E, $\langle E|V|E\rangle\approx v(E)$. The off-diagonal elements are exponentially smaller: $|\langle E|V|E'\rangle|^2\approx f(E-E')\langle V^2\rangle_{\rm micro}\exp(-S(\bar{E})/2)$, for some function f which is O(1) when the separation E-E' is small, and $\bar{E}=(E+E')/2$. $\langle V^2\rangle_{\rm micro}$ is the microcanonical value of V^2 near \bar{E} , and $S(\bar{E})=-\ln\left(\rho(\bar{E})\right)$ is the thermodynamic entropy [9]. Then the expression (S44) for the fidelity can be approximated as follows:

$$\mathbb{E}_{t}\left[F\right] = |\operatorname{tr}(\rho_{d}V)|^{2} + \operatorname{tr}\left(\rho_{d}V\rho_{d}V^{\dagger}\right) - \operatorname{tr}\left(\rho_{d}^{(2)}(V\otimes V^{\dagger})\right)$$

$$= \left|\sum_{E} \langle E|V|E\rangle \left|\langle E|\Psi_{0}\rangle\right|^{2}\right|^{2} + \sum_{E,E'} \langle E|V|E'\rangle\langle E'|V^{\dagger}|E\rangle \left|\langle E|\Psi_{0}\rangle\right|^{2} \left|\langle E'|\Psi_{0}\rangle\right|^{2} - \sum_{E} |\langle E|V|E\rangle|^{2} |\langle E|\Psi_{0}\rangle|^{4}$$
(S46)

$$\stackrel{\text{ETH}}{\approx} \left| v(\bar{E}) \right|^2 + \langle V^2 \rangle_{\text{micro}} \exp(-c'N) , \qquad (S47)$$

for some constant c' > 0.

Meanwhile, to analyze $\mathbb{E}_{\tau}\mathbb{E}_{t}\left[F_{\text{XEB,d}}(t,\tau)\right]$, we approximate $|\langle z|\rho_{d}V_{d}|z\rangle| = \sum_{E}|\langle z|E\rangle\langle E|\Psi_{0}\rangle|^{2}|\langle E|V|E\rangle| \stackrel{\text{ETF}}{\approx} \overline{\langle E|V|E\rangle}_{\bar{E}}\sum_{E}|\langle z|E\rangle\langle E|\Psi_{0}\rangle|^{2} = |v(\bar{E})|p_{\text{avg}}(z)$. Then

$$\mathbb{E}_{\tau} \mathbb{E}_{t} \left[F_{\text{XEB,d}}(t,\tau) \right] = \sum_{z} \frac{\langle z | \rho_{d} V_{d} | z \rangle \langle z | \rho_{d} V_{d}^{\dagger} | z \rangle}{p_{\text{avg}}(z)} - \sum_{z} \frac{\langle z, z | \rho_{d}^{(2)} \left(V_{d} \otimes V_{d}^{\dagger} \right) | z, z \rangle}{p_{\text{avg}}(z)} , \tag{S48}$$

$$= \sum_{z} \frac{1}{p_{\text{avg}}(z)} \left[\left| \sum_{E} \left| \langle z | E \rangle \langle E | \Psi_{0} \rangle \right|^{2} \langle E | V | E \rangle \right|^{2} - \sum_{E} \left| \langle z | E \rangle \langle E | \Psi_{0} \rangle \right|^{4} \left| \langle E | V | E \rangle \right|^{2} \right]$$
 (S49)

$$\stackrel{\text{ETH}}{\approx} \sum_{z} \frac{\left| v(\bar{E}) \right|^{2}}{p_{\text{avg}}(z)} \left[\left(\sum_{E} \left| \langle z | E \rangle \langle E | \Psi_{0} \rangle \right|^{2} \right)^{2} - \sum_{E} \left| \langle z | E \rangle \langle E | \Psi_{0} \rangle \right|^{4} \right]$$
 (S50)

$$= |v(\bar{E})|^2 (1 - D_{\beta}^{-1}) \tag{S51}$$

Since D_{β}^{-1} is also typically exponentially small in system size, we conclude that $|\mathbb{E}_{\tau}\mathbb{E}_{t}[F_{\text{XEB,d}}(t,\tau)] - \mathbb{E}_{t}[F(t)]| = O(\exp[-dN])$, for some d > 0. This is our desired result, obtained here through the ETH.

C. Variance over time

The variance over time utilizes the fourth Hamiltonian twirling identity. The proof of Theorem 2 estimates this as $O(\operatorname{tr}[\rho_d^2])$. We explicitly compute the prefactors of the expected leading order contribution arising from the simplest energy-conserving terms, illustrated in Fig. S3(b):

$$\operatorname{var}_{t}\left[F_{\mathrm{id,d}}\right] = \mathbb{E}_{t}\left[F_{\mathrm{id,d}}(t)^{2}\right] - \mathbb{E}_{t}\left[F_{\mathrm{id,d}}(t)\right]^{2} = 16\left[\operatorname{tr}\left(\rho_{d}^{2}\right) - \operatorname{tr}\left(\rho_{d}^{2}\right)\right]^{2} + 4\sum_{z,z'}\frac{\left|\langle z|\rho_{d}|z'\rangle\right|^{4}}{p_{\mathrm{avg}}(z)p_{\mathrm{avg}}(z')} + \cdots$$
(S52)

While this expression allows us to theoretically understand the expected the magnitude of $\operatorname{var}_t[F_{\operatorname{id,d}}]$, in practice we numerically evaluate $\operatorname{var}_t[F_{\operatorname{id,d}}]$ and investigate its relation to $\operatorname{var}_t[F_d]$. In the presence of errors, the variance of $F_{\operatorname{XEB,d}}$ can be calculated using Eq. (S33). This gives $\operatorname{var}_t[F_{\operatorname{XEB,d}}] \approx F^2 \operatorname{var}_t[F_{\operatorname{id,d}}]$ for incoherent errors. In the case of a *single, coherent error*, we must include the coherence of \tilde{p}_{\perp}^2 : $\langle \tilde{p}_{\perp}^2 \rangle \approx 2$ and we obtain $\operatorname{var}_t[F_{\operatorname{XEB,d}}] \approx [F^2 + (1-F)^2] \operatorname{var}_t[F_{\operatorname{id,d}}]$ instead. In both cases, we also have $\operatorname{cov}_t[F_{\operatorname{XEB,d}}, F_{\operatorname{id,d}}] \approx F \operatorname{var}_t[F_{\operatorname{id,d}}]$.

Performing the same Taylor expansion as in Eq. (S37),

$$\operatorname{var}\left[\frac{X}{Y}\right] \approx \frac{\mathbb{E}[X]^2}{\mathbb{E}[Y]^2} \left[\frac{\operatorname{var}[X]}{\mathbb{E}[X]^2} + \frac{\operatorname{var}[Y]}{\mathbb{E}[Y]^2} - 2 \frac{\operatorname{cov}[X, Y]}{\mathbb{E}[X] \mathbb{E}[Y]} \right]$$
(S53)

gives the estimate

$$\delta_{\text{temp}}^2 = \text{var}_t [F_d] \approx \frac{1}{4} (1 - F)^2 \text{var}_t [F_{\text{id,d}}] \text{ (open system dynamics)}$$
 (S54)

$$\approx \frac{5}{4} (1 - F)^2 \text{var}_t [F_{\text{id,d}}] \text{ (coherent errors)}$$
 (S55)

(a)
$$\begin{bmatrix} z \\ t \end{bmatrix} \begin{bmatrix} z \\ t \end{bmatrix} \begin{bmatrix} z \\ t \\ z \end{bmatrix} \begin{bmatrix} z \\ t \\ t \\ z \end{bmatrix} \begin{bmatrix} z \\ t \\ t \\ z \end{bmatrix} \begin{bmatrix} z \\ t \\ t \\ z \end{bmatrix} \begin{bmatrix} z \\ t \\ t \\ z \end{bmatrix} \begin{bmatrix} z \\ t \\ t \\ z \end{bmatrix} \begin{bmatrix} z \\ t \\ t \\ z \end{bmatrix} \begin{bmatrix} z \\ t \\ t \\ t \\ z \end{bmatrix} \begin{bmatrix} z \\ t \\ t \\ t \\ t \end{bmatrix} \begin{bmatrix} z \\ t \\ t \\ t \\ t \\ t \end{bmatrix} \begin{bmatrix} z \\ t \\ t \\ t \\ t \\ t \end{bmatrix} \begin{bmatrix} z \\ t \\ t \\ t \\ t \\ t \end{bmatrix} \begin{bmatrix} z \\ t \\ t \\ t \\ t \\ t \end{bmatrix} \begin{bmatrix} z \\ t \\ t \\ t \\ t \\ t \end{bmatrix} \begin{bmatrix} z \\ t \\ t \\ t \\ t \\ t \end{bmatrix} \begin{bmatrix} z \\ t \\ t \\ t \\ t \\ t \end{bmatrix} \begin{bmatrix} z \\ t \\ t \\ t \\ t \\ t \\ t \end{bmatrix} \begin{bmatrix} z \\ t \\ t \\ t \\ t \\ t \\ t \end{bmatrix} \begin{bmatrix} z \\ t \\ t \\ t \\ t \\ t \\ t \end{bmatrix} \begin{bmatrix} z \\ t \\ t \\ t \\ t \\ t \\ t \end{bmatrix} \begin{bmatrix} z \\ t \\ t \\ t \\ t \\ t \\ t \end{bmatrix} \begin{bmatrix} z \\ t \\ t \\ t \\ t \\ t \end{bmatrix} \begin{bmatrix} z \\ t \\ t \\ t \\ t \\ t \end{bmatrix} \begin{bmatrix} z \\ t \\ t \\ t \\ t \\ t \end{bmatrix} \begin{bmatrix} z \\ t \\ t \\ t \\ t \\ t \end{bmatrix} \begin{bmatrix} z \\ t \\ t \\ t \\ t \\ t \end{bmatrix} \begin{bmatrix} z \\ t \\ t \\ t \\ t \\ t \end{bmatrix} \begin{bmatrix} z \\ t \\ t \\ t \\ t \end{bmatrix} \begin{bmatrix} z \\ t \\ t \\ t \end{bmatrix} \begin{bmatrix} z \\ t \\ t \\ t \\ t \end{bmatrix} \begin{bmatrix} z \\ t \\ t \\ t \end{bmatrix} \begin{bmatrix} z \\ t \\ t \\ t \end{bmatrix} \begin{bmatrix} z \\ t \\ t \\ t \end{bmatrix} \begin{bmatrix} z \\ t \\ t \\ t \end{bmatrix} \begin{bmatrix} z \\ t \\ t \\ t \end{bmatrix} \begin{bmatrix} z \\ t \\ t \\ t \end{bmatrix} \begin{bmatrix} z \\ t \\ t \\ t \end{bmatrix} \begin{bmatrix} z \\ t \\ t \\ t \end{bmatrix} \begin{bmatrix} z \\ t \\ t \\ t \end{bmatrix} \begin{bmatrix} z \\ t \\ t \\ t \end{bmatrix} \begin{bmatrix} z \\ t \\ t \end{bmatrix} \begin{bmatrix} z \\ t \\ t \\ t \end{bmatrix} \begin{bmatrix} z \\ t \end{bmatrix} \begin{bmatrix} z \\ t \\ t \end{bmatrix} \begin{bmatrix} z \\ t$$

Figure S3. Diagrammatic derivation of terms that contribute to (a) $\mathbb{E}_t[F_{\mathrm{id,d}}(t)]$ and (b) $\mathrm{var}_t[F_{\mathrm{id,d}}(t)]$. In (a), the two permutations and collision term give $2-D_\beta^{-1}$. In (b), we list the (expected) leading order contributions. 16 out of the 24 possible permutations each give $\mathrm{tr}(\rho_d^2)$, these are cancelled out by corresponding collision terms: representative permutations and collision terms are illustrated here. Another four permutations give the leading order contribution to $\mathrm{var}_t[F_{\mathrm{id,d}}(t)] = 4\sum_{z,z'}|\langle z|\rho_d\,|z'\rangle|^4/(p_{\mathrm{avg}}(z)p_{\mathrm{avg}}(z')) \leq 4\,\mathrm{tr}(\rho_d^2)$.

Here, the larger fluctuations for a single coherent error are associated with the fact that it is pure. We numerically evaluate $\operatorname{var}_t[F_{\mathrm{id,d}}]^{-1}$, and compare our predictions for $\operatorname{var}_t[F_d]$ in terms of $\operatorname{var}_t[F_{\mathrm{id,d}}]$ and F in Fig. 2(c) of the main text and Fig. S4(b,d) (respectively single error and open system dynamics).

D. Sample complexity

The sample complexity of F_d is related to the variance of the estimator \hat{F}_d with a finite number of samples M. The variance δ_{stat}^2 is given by

$$\delta_{\text{stat}}^2 \equiv \text{var}\big[\hat{F}_d\big] = \frac{4\left(\sum_z q(z)\tilde{p}(z)^2 - \left[\sum_z q(z)\tilde{p}(z)\right]^2\right)}{M\left[\sum_z p_{\text{avg}}(z)\tilde{p}(z)^2\right]^2} \overset{\text{large } t}{\approx} \frac{1}{M} \left(\sum_z q(z)\tilde{p}(z)^2 - \left[\sum_z q(z)\tilde{p}(z)\right]^2\right) \tag{S56}$$

We estimate this by computing computing its time-averaged value, with the third Hamiltonian twirling identity, which gives $\mathbb{E}_t \left[\sum_z p_{\text{avg}}(z) \tilde{p}(z,t)^3 \right] = 3! - (2!)^2 + \cdots \approx 2$. Our ansatz for $\tilde{q}(z,t)$ (S33) gives:

$$\mathbb{E}_{t}\left[M\delta_{\text{stat}}^{2}\right] = \mathbb{E}_{t}\left[\sum_{z} p_{\text{avg}}(z)\tilde{q}(z,t)\tilde{p}(z,t)^{2} - \left(\sum_{z} p_{\text{avg}}(z)\tilde{q}(z,t)\tilde{p}(z,t)\right)^{2}\right] \approx 1 + 2F - F^{2}. \tag{S57}$$

This non-trivial prediction is verified in Fig. S4(c) and Fig. 2(d) of the main text.

E. Moderate error rate: Effects of delay time τ_d

Here we argue that under open system dynamics with a moderate error rate, the ratio F_d/F approaches a constant $F_d/F \approx \exp(\gamma \tau_d)$, where γ is the total error-rate and τ_d is a response time independent of system size. When the fidelity F shows a simple exponential decay, the delay time leads to F_d lagging behind F by a constant time τ_d . This is in contrast to the constant difference $F_d - F$ seen under a single error, which is exponentially small in system size. We quantify this delay time effect by introducing the notion of a response function of F_d after a single error, $F_d^{(1)}$, and making the assumption that the effects of multiple errors on F_d are independent and factorize.

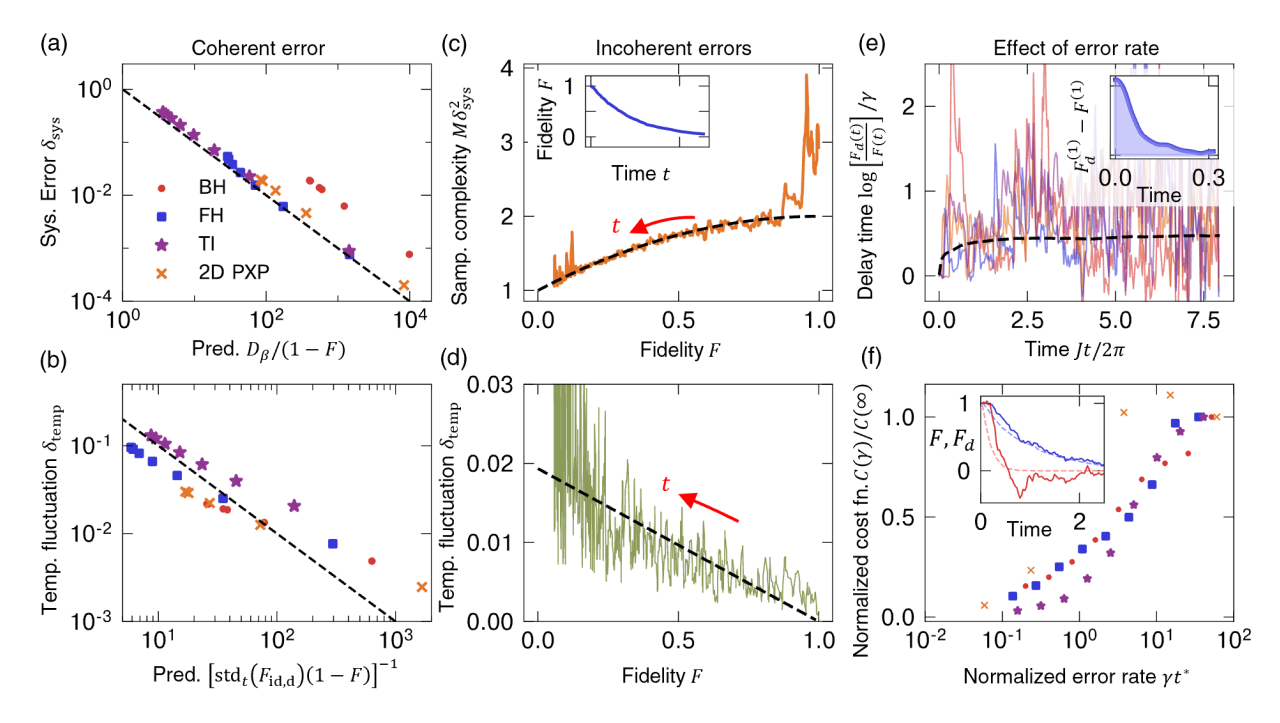


Figure S4. Performance metrics for F_d under single and continuous errors. In all cases, our numerical results quantitatively agree with our theoretical predictions (black dashed lines), with all parameters numerically extracted from independent numerical data. (a,b) After a single error, the (a) systematic error $\delta_{sys.}$ and (b) temporal standard deviation $\delta_{temp.}$ quantitatively agrees with the ansatz $\delta_{\text{sys.}} = (1 - F)D_{\beta}^{-1}$ and $\delta_{\text{temp.}} = \sqrt{5/4}(1 - F)\text{std}_t [F_{\text{id,d}}]$, across all four systems studied: a Bose-Hubbard model (red), Fermi-Hubbard model (blue), trapped-ion spin chain Hamiltonian (purple), and 2D Rydberg model (orange). (c,d) In the presence of continuous errors, F decays with time from 1 to 0 (inset). Therefore, we can test our predictions for the dependence of our quantities of interest—the sample complexity (c), and the temporal fluctuations (d)—on the fidelity F in a single time series of open system dynamics. We present such a time series for a Bose-Hubbard model with 8 bosons on 8 sites, where we plot the (c) sample complexity at each point in time and the (d) temporal fluctuations in a narrow time window against the fidelity F at that point in time. After a short thermalization time, the sample complexity follows our universal prediction in Eq. (S57): $M\delta_{\text{stat.}}^2 = (1 + 2F - F^2)$, and the temporal fluctuations satisfy Eq. (S54): $\delta_{\text{temp.}} = (1 - F) \text{std}_t [F_{\text{id,d}}] / 2$. (e) Under continuous errors, $F_d(t)$ will appear to lag behind F(t) with a delay time. In particular, the rescaled curves of F_d/F for a range of error rates $\gamma = 0.0005$ to $\gamma = 0.005$ collapse, and are close to our prediction in Eq. (S60), obtained from the single-error response curve (inset). (f) At low error rates, F_d estimates F well, but they deviate significantly at high error rates. Inset: Across all platforms, a normalized cost function $C(\gamma)/C(\infty)$ (S63) shows a crossover when the average time between errors is less than an error autocorrelation time t^* (S62).

We assume that an error operator X can occur at any time during the open system dynamics. Without loss of generality, we normalize X so it does not change the norm of a typical state: $\langle \psi(t)|X^{\dagger}X|\psi(t)\rangle \approx 1$. The fidelity F as a function of time is:

$$F(t) \approx p_{ne}(t) + \int_0^t dt_1 p_e(t_1) |\langle X(t_1) \rangle|^2 + \int_0^t dt_1 \int_{t_1}^t dt_2 p_e(t_1, t_2) |\langle X(t_2) X(t_1) \rangle|^2 + \cdots$$

$$\approx p_{ne} + \sum_{n=1}^\infty \frac{1}{n!} \left[\int_0^t dt_i p_e(t_i) |\langle X(t_i) \rangle|^2 \right]^n = \exp[(F_\beta - 1) \gamma t] , \qquad (S58)$$

where we denote $p_{ne}(t) \propto \exp(-\gamma t)$ as the probability of not having an error from time 0 to t and $p_e(t_1, \dots, t_n) \propto \gamma^n$ as the probability density of errors occurring at times t_1, \dots, t_n . If n errors occur during a trajectory, the pure state assponded with this trajectory will have a fidelity $\left| \langle \psi(t_n) | X \cdots X e^{-iH(t_2-t_1)} X | \psi(t_1) \rangle \right|^2$. As long as the error rate is low enough that errors are typically far apart in time, we assume that this expression factorizes: $F = |\langle X(t_n) \cdots X(t_1) \rangle|^2 \approx |\langle X \rangle|_\beta^2 \equiv F_\beta^n$. Here the quantity $F_\beta \equiv |\langle X \rangle|_\beta^2$ should be interpreted as the fidelity after a single error X on a typical thermal state.

Meanwhile, we can estimate how F_d behaves under open system dynamics in terms of its behavior in response to a single error. We denote $F_d^{(1)}(\tau)$ as the average F_d value at time τ after a single error.

$$F_d(t) \approx p_{ne}(t) + \int_0^t dt_1 p_e(t_1) F_d(t - t_1) + \int_0^t \int_{t_1}^t dt_1 dt_2 p_e(t_1, t_2) F_d(t - t_2, t - t_1) + \cdots$$

$$\approx p_{ne} + \sum_{n=1}^\infty \frac{1}{n!} \left[\int_0^t dt_i p_e(t_i) F_d^{(1)}(t - t_i) \right]^n = \exp\left[\gamma \int_0^t d\tau \left(F_d^{(1)}(\tau) - 1 \right) \right]$$
(S59)

where we again assume that the value of F_d after n errors factorizes as: $F_d(t_1, \dots, t_n) \approx \prod_i F_d^{(1)}(t - t_i)$. Combining Eqs. (S58), (S59), we have a simple expression for the ratios:

$$\frac{F_d(t)}{F(t)} \approx \exp\left[\gamma \int_0^t d\tau \left(F_d^{(1)}(\tau) - F_\beta\right)\right] \approx \exp[\gamma \tau_d] , \qquad (S60)$$

where the quantity $\tau_d \equiv \int_0^\infty d\tau \left(F_d^{(1)}(\tau) - F_\beta\right) dt$ has a natural interpretation as the total area under the response curve $F_d^{(1)}(\tau) - F_\beta$ (Fig. S4(e) inset) — if we ignore the (exponentially small) systematic error $\bar{F}_d^{(1)} - F$, this total area is a constant. This prediction is supported in Fig. S4(e), where we observe the ratio $F_d(t)/F$ saturating at our predicted value for $\exp[\gamma \tau_d]$, with τ_d extracted from the corresponding single error curve $F_d^{(1)}(t)$.

F. Large error rate: Critical error rate and operator scrambling time

As the error rate increases, there is a critical rate at which F_d shows significant deviations from F [Fig. S4(f) inset]. Naively, we would expect that this error rate is solely determined by the delay time discussed above. However, this is not necessarily the case. The delay time is a property of the relaxation dynamics of a local perturbation occurring after the state has reached thermal equilibrium. When the error rate is substantially larger than the local relaxation time, the fidelity becomes very small even before the state has a chance to reach thermal equilibrium. Therefore, the delay time might not be the appropriate timescale for the critical error rate. Instead, we seek to characterize a different timescale relevant in this non-equilibrium dynamics. We hypothesize that a suitable timescale is the error operator autocorrelation time — intuitively an operator scrambling time — t^* with respect to the nonequilibrium initial state. Our numerical results support our hypothesis: we find that the critical error rate is related to t^* .

We define the autocorrelation function of the error operator X_j , for a given initial state $|\Psi_0\rangle$ and quench Hamiltonian H, as:

$$A_j(t) = \frac{\left| \langle \Psi_0 | e^{iHt} X_j e^{-iHt} X_j | \Psi_0 \rangle \right|^2}{\langle \Psi_0 | e^{iHt} X_j^2 e^{-iHt} | \Psi_0 \rangle \langle \Psi_0 | X_j^2 | \Psi_0 \rangle} , \tag{S61}$$

where we have chosen this normalization such that $0 \le A(t) \le 1$. The states $X_j | \Psi(t) \rangle$ are generally not normalized because the error operators X_j may not be unitary (for example, in the Bose-Hubbard model, the errors are associated with photon scattering, and we take X_j to be n_j). We define the autocorrelation time as:

$$t_j^* \equiv \frac{\int_0^\infty dt |A_j(t) - A_j(\infty)|}{1 - A_j(\infty)} , \qquad (S62)$$

where $A_j(\infty)$ is the infinite time value $A_j(\infty) = \lim_{t\to\infty} A_j(t)$. This can be analytically evaluated from the second Hamiltonian twirling identity [Eq. (S2)]. We take the overall operator scrambling time as the average of t_j^* over error operators X_j . This timescale is independent of system size, unlike other timescales such as the time for the entanglement entropy to saturate, which scales with system size.

Importantly, we find that the critical error rate is associated with the non-equilibrium dynamics of the initial state, as opposed to the dynamics after the state has reached thermal equilibrium. To numerically demonstrate this, we initialize the noisy dynamics on a time-evolved state $e^{-iHt} |\Psi_0\rangle$ for sufficiently large t, after the state has thermalized. We find that in the regime of error rates studied, there is no critical change in the accuracy of F_d , merely a constant delay time between F_d and F, as predicted in Section II E, which translates to a smooth increase in the relative error F_d/F . This is analogous to Ref. [10, 11], in which the error rate in random unitary circuits was found to have the largest effect at the start and the end of the evolution.

We define a cost function

$$C(\gamma) \equiv \int_0^T dt |F_d(t) - F(t)| , \qquad (S63)$$

that captures the total deviation between F_d and F over time. In Fig. S4(f), we find that the rescaled cost function $C(\gamma)/C(\infty)$ shows a crossover from 0 to 1 at $\gamma t^* \sim 1$, indicating that t^* is the relevant timescale for our setting. We choose such a normalization such that the curves from different simulator platforms can be plotted on the same graph: they demonstrate a cross over in a common regime $\gamma t^* \sim 1$.

G. Symmetry Resolution

In the main text, we described how F_d naturally incorporates symmetries of the quench Hamiltonian. Here, we discuss this in more detail and provide an explicit example. If the initial state belongs to a single symmetry sector s, the quenched state will remain in that sector. Assume for simplicity that the state is Haar random in s. The simpler formulae F_{XEB} and F_c would be appropriate if our measurements z were also states in s. However, this is generically not the case — if the outcome z does not have a well-defined symmetry quantum number, it should be weighted by its overlap with s. The factor $p_{\text{avg}}(z)$ automatically weights z appropriately, without explicit knowledge of the symmetry. As an illustration, consider spatial inversion symmetry \mathcal{I} on a lattice. The even parity sector has basis states $|e_z\rangle = \mathcal{N}(|z\rangle + |\bar{z}\rangle)$, where \bar{z} is the mirrored configuration of z. If $\bar{z} = z$, $\mathcal{N} = 1/2$, otherwise $\mathcal{N} = 1/\sqrt{2}$. Consider the optimal case where $|\Psi_0\rangle$ is a random even-parity state and the dynamics is a random unitary that conserves parity. The universal statistics would be apparent if we could measure in the $\{|e_z\rangle\}$ basis — a challenging task. Instead, outcome configurations z have unequal average probabilities: $p_{\text{avg}}(z) = 1/D_s$ if $z = \bar{z}$ and $p_{\text{avg}}(z) = 1/(2D_s)$ otherwise, where D_s is the dimension of the symmetry sector. While p(z) does not follow the Porter-Thomas distribution, $\tilde{p}(z)$ does. Therefore, F_d correctly estimates F, while F_c unequally weights some basis states. This argument generalizes to other symmetries such as translational invariance. Since $p_{\text{avg}}(z)$ automatically accounts for symmetries, our conclusions hold even in the presence of extensively many symmetries, as in the case of integrable systems. Finally, in a special case where the readout basis states have well-defined symmetry quantum number, F_d does not estimate F. This is discussed in Section VG.

H. Alternative fidelity estimator F_e

In the following section, we use the random MPS model to derive another fidelity estimator $F_e \equiv (\sum_z p_{\text{avg}}(z)\tilde{q}(z)\tilde{p}(z) - 1)/(\sum_z p_{\text{avg}}(z)\tilde{p}(z)^2 - 1) = F_{\text{XEB,d}}/F_{\text{id,d}}$. Here, we summarize some of its properties. While the temporal fluctuations and sample complexity of F_e are similar to those of F_d , the systematic error (after a long time) is smaller.

- (i) Systematic error. The analysis in Section IIB indicates that the systematic error after a single error $\delta_{\text{sys}} = \mathbb{E}_t F_d(t) F = O(D_{\beta}^{-1})$. Repeating the same analysis for F_e indicates that the systematic error vanishes for F_e , to first order. This indicates that F_e is less sensitive to small values of D_{β} , and hence may perform better in quench dynamics with low effective temperature. This is supported in Fig. S6(e,f). More fundamentally, F_e is more robust against deviations of the denominator $\sum_z p_{\text{avg}}(z)\tilde{p}(z)^2$ from 2. For example, in the presence of particle hole symmetry, this denominator can be 3. F_d can be appropriately modified to take this into account, but F_e estimates the fidelity without any modification [Fig. S6(a,b)].
- (ii) Non-local errors. Our analysis based on random matrix product states indicates that F_e will estimate F for highly non-local errors. This is numerically supported in Fig. S7(f).
- (iii) Short-time response. A tradeoff of F_e is that it typically has a longer response time than F_d to learn the fidelity F. This is demonstrated in Fig. S7(e) and Fig. S8(b).

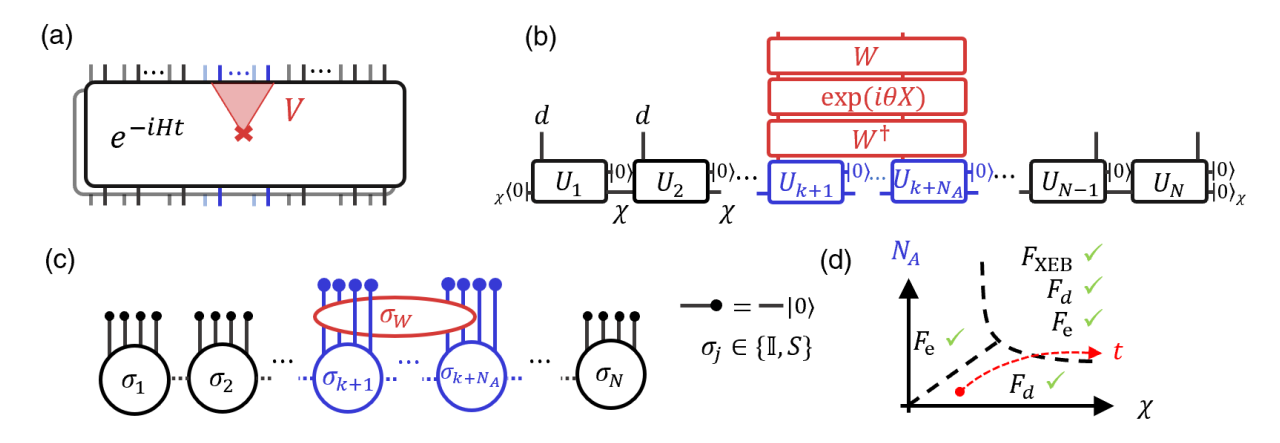


Figure S5. Random matrix product state model. (a) We consider two states evolved by a short quench. In one copy, an error has occurred, which spreads to a small subsystem A, and no error has occurred in the other copy. (b) A toy model for the non-equilibrium state is the random MPS — a matrix product state with a random $\chi d \times \chi d$ matrix at every site, with χ the MPS bond dimension, and d the local Hilbert space. The error V is also modeled with a random unitary W and an operator $\exp(i\theta X)$. (c) The expression for F_d , averaged over random unitaries is mapped to the partition function of an effective ferromagnetic Ising spin chain, with Ising degrees of freedom σ_j , $\sigma_W \in \{\mathbb{I}, \mathcal{S}\}$. This partition function is given in Eq. (S65). (d) We predict regimes of validity for our benchmarking formulae F_d , F_e , and F_{XEB} , depending on the error operator size N_A and MPS bond dimension χ . A typical quench is always in the regime of validity of F_d (red arrow).

III. DETAILED PERFORMANCE ANALYSIS FOR SHORT QUENCH DYNAMICS

A. Overview: random matrix product states

The infinite-time averaging in Section II tells us that our fidelity estimators work at late times. Our formulae are also designed to work at early times, before the state has reached equilibrium. To capture this early time physics, we introduce a toy model, the *random matrix product state*.

We model the state $|\Psi_0(t)\rangle$ as a matrix product state (MPS) with bond dimension χ and local Hilbert space dimension d. The MPS is constructed by choosing a $\chi d \times \chi d$ random unitary U_j on each site j, as illustrated in Fig. S5(b). At every site, a d degree of freedom is eliminated by contracting to the state $|0\rangle$. At the boundary sites, an additional χ degree of freedom is removed by contracting to a state $|0\rangle_{\chi}$ on the bond-dimension space. This provides a toy model for a state with entanglement $S \sim \log(\chi)$. Because of its random unitary nature, there are no systematic patterns in p(z,t): $p_{\text{avg}}(z) = 1/D$. Therefore, F_d agrees with F_c in this case.

We model the error operator V as $V = W \exp(i\theta X) W^{\dagger}$, where V is taken to be supported on some region A, and W is a random unitary on \mathcal{H}_A . $\exp(i\theta X)$ is an operator whose precise form will be irrelevant. However, the parameter θ measures the strength of the coherent error, and can be used to tune the fidelity between the perturbed and initial states. The random unitary W models the scrambling nature of $V(\tau)$ while making the calculation tractable using techniques of averaging over random unitaries [12].

This toy model captures what we believe to be the essential physics: entanglement and operator growth. In particular, it is well known that both entanglement entropy and operator size grow linearly with time. This corresponds to:

$$\chi \sim \exp(v_S t) , N_A \sim v t ,$$
(S64)

where v_S is an entanglement velocity, and v is an operator spreading velocity [13, 14].

Our calculations give us expressions for how $F_{\text{XEB}} \equiv \sum_z q(z)p(z) - 1$ and $F_{\text{id}} \equiv \sum_z p(z)^2 - 1$, and the fidelity F depend on N_A and χ . Our estimators F_d and F_e , in our case where $p_{\text{avg}}(z)$ is constant, are given by $F_d = 2(F_{\text{XEB}} + 1)/(F_{\text{id}} + 1) - 1$ and $F_e = F_{\text{XEB}}/F_{\text{id}}$. Our main result is:

$$\mathbb{E}_{W,\mathbf{U}}\left[F_{\text{XEB}} + 1\right] \approx \mathbb{E}_{\mathbf{U}}\left[F_{\text{id}} + 1\right] \left(F + \exp\left[-\frac{d-1}{d}\frac{N_A}{\chi}\right] \frac{1-F}{2}\right) , \tag{S65}$$

where $\mathbb{E}_{W,\mathbf{U}}$ denotes averaging over the random unitaries W and $\mathbf{U} = \{U_j\}$, and $\mathbb{E}_{\mathbf{U}}$ denotes averaging over \mathbf{U} . The second term describes a crossover between two regimes: $\chi \ll N_A$ and $\chi \gg N_A$. In the former regime, $\exp\left[-\frac{d-1}{d}\frac{N_A}{\chi}\right] \approx 0$, and $F_{\text{XEB}} + 1 \approx (F_{\text{id}} + 1) F$. Furthermore since χ is small, both F_{id} and F_{XEB} are exponentially large and

$$F \approx \frac{F_{\text{XEB}} + 1}{F_{\text{id}} + 1} \approx \frac{F_{\text{XEB}}}{F_{\text{id}}} = F_e . \tag{S66}$$

In the latter regime, $\exp\left[-\frac{d-1}{d}\frac{N_A}{\chi}\right]\approx 1$, and $F_{\rm XEB}+1\approx (F_{\rm id}+1)\frac{1+F}{2}$, and

$$F \approx 2 \frac{F_{\text{XEB}} + 1}{F_{\text{id}} + 1} - 1 = F_d$$
 (S67)

Both F_d and $F_e \equiv \left[\sum_z p_{\rm avg}(z) \tilde{q}(z) \tilde{p}(z) - 1\right] / \left[\sum_z p_{\rm avg}(z) \tilde{p}(z)^2 - 1\right]$ accurately estimate F at late times. F_d is valid since $\chi \approx D \gg N_A$. However F_e is also valid since $F_{\rm id} \approx 1$ and so $F_{\rm XEB} \approx F$. These results give the regime of validity of F_d and F_e sketched in Fig. S5(d). Further properties of F_e are discussed in Sec. II H.

B. Remarks

The random MPS model qualitatively captures the short time physics. However, it is not quantitatively accurate, at least to first order in D^{-1} . The simplest example of this is that the state norm has non-zero variance: $\operatorname{var}_{\mathbf{U}}\left[|\langle\Psi_{\mathbf{U}}|\Psi_{\mathbf{U}}\rangle|^2\right]\neq 0$. As another example, F_{id} is, on average, bigger than 1, while $\mathbb{E}_t\left[F_{\mathrm{id,d}}\right]\leq 1$ for Hamiltonian dynamics [Eq. (S35)]. Furthermore, the randomness in the MPS does not capture the systematic trends in finite temperature states that lead to non-trivial $p_{\mathrm{avg}}(z)$ factors. Therefore, the random MPS model cannot be a qualitative model for non-equilibrium quench-evolved states at either finite or infinite temperature. Nevertheless, the qualitative conclusions of the random MPS model — in particular the regimes of validity of F_d and F_e — are consistent with numerical results at finite temperature.

C. Derivation of result

We model the error operator $V(\tau) = We^{i\theta X}W^{\dagger}$, where W is a Haar-random unitary supported on A [Fig. S5(b)]. This models the effect of scrambling and makes the calculation tractable. We first integrate over W (a unitary two-design calculation [6, 12]), and obtain two terms corresponding to the permutations of two elements: $\sigma_W = \mathbb{I}$ and $\sigma_W = \mathcal{S}$. We then integrate over U to obtain effective Ising chains for each value of σ_W : the integration over unitaries U_j leaves a degree of freedom on each sites with two possible states, again corresponding to (local) \mathbb{I} and \mathcal{S} permutations [Fig. S5(c)]. These degrees of freedom "interact" with their nearest neighbors ferromagnetically: the lowest energy configurations are those with all sites in the \mathbb{I} state or all sites in the \mathcal{S} state. This ferromagnetic interaction is encoded in the transfer matrix (of the partition function) T_0 (S71).

The presence of the error operator $V(\tau)$ modifies this effective Ising chain when $\sigma_W = \mathcal{S}$: it introduces an effective magnetic field on the region A supporting the error.

Our quantities of interest can be expressed in terms of the partition functions of these two Ising chains. We call these partition functions $f_{X,\mathbb{I}}$ and $f_{X,\mathcal{S}}$, corresponding to the value of σ_W . For example, the average value of $F_{\mathrm{id}} + 1$ over all possible choices of U_j is exactly the partition function $f_{X,\mathbb{I}}$. The presence of an error changes the value of $F_{\mathrm{XEB}} + 1$. $F_{\mathrm{XEB}} + 1$, again averaged over unitaries U_j and W, can be expressed in terms of $f_{X,\mathbb{I}}$, $f_{X,\mathcal{S}}$, and the (averaged) fidelity F.

Our calculation gives the expressions:

$$\mathbb{E}_{W,\mathbf{U}}\left[F\right] = \frac{\left|\operatorname{tr}V\right|^{2} - 1}{D_{A}^{2} - 1} \mathbb{E}_{\mathbf{U}}\left[\left|\left\langle\Psi_{\mathbf{U}}|\Psi_{\mathbf{U}}\right\rangle\right|^{2}\right] + \frac{\left|D_{A}^{2} - \operatorname{tr}V\right|^{2}}{D_{A}\left(D_{A}^{2} - 1\right)} \mathbb{E}_{\mathbf{U}}\left[\operatorname{tr}\left(\rho_{A}^{2}\right)\right] \approx \frac{\left|\operatorname{tr}V\right|^{2} - 1}{D_{A}^{2} - 1} \equiv \bar{F} , \tag{S68}$$

$$\mathbb{E}_{W,\mathbf{U}}\left[F_{\text{XEB}} + 1\right] = f_{X,\mathbb{I}}\bar{F} + \frac{f_{X,\mathcal{S}}}{D_A}\left(1 - \bar{F}\right) , \qquad (S69)$$

$$\mathbb{E}_{\mathbf{U}}\left[F_{\mathrm{id}}+1\right] = f_{X,\mathbb{I}} , \qquad (S70)$$

where the coefficients $f_{X,\mathbb{I}}$ and $f_{X,\mathcal{S}}$ are the partition functions of the Ising spin models, defined by the transfer matrices:

$$T_0 = \frac{1}{\chi^2 d^2 - 1} \begin{pmatrix} \chi^2 d^2 - d & \chi d(d-1) \\ \chi d(d-1) & \chi^2 d^2 - d \end{pmatrix} , T_1 = \begin{pmatrix} 1 & 0 \\ 0 & \sqrt{d} \end{pmatrix} T_0 \begin{pmatrix} 1 & 0 \\ 0 & \sqrt{d} \end{pmatrix} . \tag{S71}$$

These transfer matrices are obtained from the Weingarten coefficients that arise from the integration over random unitaries [12]. The partition functions are

$$f_{X,\mathbb{I}} \equiv \frac{\chi}{\chi + 1} \frac{\chi d + d}{\chi d + 1} \begin{pmatrix} 1 & 1 \end{pmatrix} T_0^{N-1} \begin{pmatrix} 1 \\ 1 \end{pmatrix} = 2 \frac{\chi}{\chi + 1} \left(\frac{\chi d + d}{\chi d + 1} \right)^N , \qquad (S72)$$

$$f_{X,S} \equiv \frac{\chi}{\chi + 1} \frac{\chi d + d}{\chi d + 1} \begin{pmatrix} 1 & 1 \end{pmatrix} T_0^{k-1} \begin{pmatrix} 1 & 0 \\ 0 & \sqrt{d} \end{pmatrix} T_1^{N_A} \begin{pmatrix} 1 & 0 \\ 0 & \sqrt{d} \end{pmatrix} T_0^{N-N_A-k} \begin{pmatrix} 1 \\ 1 \end{pmatrix} . \tag{S73}$$

As a reminder, $f_{X,\mathbb{I}}$ is the partition function of the ferromagnetic effective Ising model, while $f_{X,\mathcal{S}}$ is the partition function of the same Ising spin chain with an additional (very strong) effective magnetic field applied on region A, that effectively locks all the Ising spins in A to the swap state \mathcal{S} .

We can simplify $f_{X,\mathbb{I}}$ and $f_{X,\mathcal{S}}$ by noting that the dominant contributions to $f_{X,\mathbb{I}}$ are the configurations with all sites in the \mathbb{I} state, and all sites in the \mathcal{S} state. Meanwhile, the dominant contribution to $f_{X,\mathcal{S}}$ is the configuration with all sites in the \mathcal{S} state. Furthermore, T_0 has eigenvalues $\frac{\chi d-d}{\chi d-1}$ and $\frac{\chi d+d}{\chi d+1}$, while T_1 has eigenvalues $\frac{(\chi d)^2-d^2}{(\chi d)^2-1}$ and d. Therefore, for large N_A , $\frac{f_{X,\mathcal{S}}}{D_A f_{X,\mathbb{I}}}$ is proportional to the ratio of their largest eigenvalues:

$$\frac{1}{D_A} \frac{f_{X,\mathcal{S}}}{f_{X,\mathbb{I}}} \approx \frac{1}{2} \left(\frac{\chi d + 1}{\chi d + d} \right)^{N_A} \approx \frac{1}{2} \exp\left(-\frac{d - 1}{d} \frac{N_A}{\chi} \right). \tag{S74}$$

where the factor of a half comes from the breaking of the global Ising $\mathbb{I} \leftrightarrow \mathcal{S}$ symmetry.

This gives our main result Eq. (S65), which predicts the relationship between the cross-entropy benchmark F_{XEB} , fidelity, and the parameters in our model: the operator size N_A and MPS bond dimension χ .

IV. DETAILS OF NUMERICAL SIMULATIONS

Below we summarize the details of the models simulated: their Hamiltonians, initial states, error models, and Hamiltonian parameter values.

A. Bose-Hubbard model

We numerically simulate quench evolution under the one-dimensional (1D) Bose-Hubbard Hamiltonian [15] in the presence of noise, which is often dominated by the photon scattering from optical lattices. In the quantum trajectory formalism [16], such noisy dynamics is described by stochastically applying the particle number operator $\{n_j\}$ at a rate γ for each site. An ensemble of such pure state evolution represents a mixed state $\rho(t)$ in open dynamics. The 1D Bose-Hubbard Hamiltonian is:

$$H_{\rm BH} = -J \sum_{j=1}^{N-1} \left(b_j^{\dagger} b_{j+1} + \text{h.c.} \right) + \frac{U}{2} \sum_{j=1}^{N} n_j (n_j - 1) , \qquad (S75)$$

where b_j^{\dagger} is the bosonic creation operator at site j, and $n_j = b_j^{\dagger} b_j$ is the bosonic number operator at site j. To increase the ergodicity of our quench, we choose the parameters (U, J) = (1, 0.5), whose ground state is in the superfluid phase. We take as initial state the "unity filling state" $|1, 1, \ldots, 1\rangle$, which is the ground state deep in the Mott insulating phase $U \gg J$.

Our error operators are $\{n_j\}$, which model the effects of scattering from optical lattice photons [17]. In Fig. 1(c), we use an overall error rate of $\gamma = 0.05$ in a system with 10 bosons on 10 sites (with total Hilbert space dimension 92378).

1. Disorder Averaging

In Fig. 2(b-d), we present disorder averaged results for the response curve and the sample complexity of F_d against time. Disorder averaging is done to remove the large fluctuations present at short times in order to clearly observe systematic behavior.

For simplicity, we choose the following ensemble of Bose-Hubbard models with disordered hopping strengths:

$$H_{\rm BH} = -\sum_{j=1}^{N-1} J_j \left(b_j^{\dagger} b_{j+1} + \text{h.c.} \right) + \frac{U}{2} \sum_{j=1}^{N} n_j (n_j - 1) , \qquad (S76)$$

with $J_j = 0.2m_j$, for m_j a random integer from 1 to 10. As in Eq. (S76), we choose U = 0.5. We chose to disorder the hopping strengths in order to observe different dynamics at short terms. If, for example, we had chosen a disordered potential $\Delta_j n_j$ instead, due to the homegeneous initial state $|1, \ldots, 1\rangle$, the resultant states $|\psi(t)\rangle$ would not be significantly different from each other across disorder realizations. Lastly, an error at $n_{\lfloor L/2 \rfloor}$ is applied at a fixed, early time t = 5J. This is because the error operator n_j acts trivially on the initial state $|1, \ldots, 1\rangle$.

B. Fermi-Hubbard model

The 1D Fermi-Hubbard model Hamiltonian is:

$$H_{\text{FH}} = \sum_{j=1}^{N} \left[-t \sum_{\sigma = \uparrow, \downarrow} \left(c_{j,\sigma}^{\dagger} c_{j+1,\sigma} + \text{h.c.} \right) + U n_{j,\uparrow} n_{j,\downarrow} \right] , \qquad (S77)$$

where $c_{j,\sigma}^{\dagger}$ is the creation operator of a fermion at site j, with spin $\sigma \in \{\uparrow, \downarrow\}$, and $n_{j,\sigma} = c_{j,\sigma}^{\dagger} c_{j,\sigma} \in \{0,1\}$ is the fermion occupation number. We use parameters (t,U) = (1,1). For any value of U/t, this model is integrable by Bethe Ansatz [18], but we numerically observe that it still passes the 2nd no-resonance condition, after disregarding degeneracies [Eq. (S1)]. As discussed in Section I, degeneracies can be disregarded for the purposes of Theorem 2.

We take as initial state the anti-ferromagnetic state at half filling, $|\uparrow,\downarrow,\ldots\rangle$, and as error operators the total fermion occupation $\{n_{j,\uparrow}+n_{j,\downarrow}\}$ at each site. As with the Bose-Hubbard model, this models scattering from optical lattice photons [19]. In Fig. 1(d), we use a total error rate of $\gamma = 0.2$, in a system with 5 up and 5 down fermions on 10 sites (with total Hilbert space dimension 63504).

C. Trapped ion model

Our trapped ion model has Hamiltonian:

with σ_j^x and σ_j^z the Pauli x- and z-operators on site j. $H_{\rm TI}$ is adapted from the experiment of Ref. [20]. Due to the long-ranged interactions, following Ref. [20] we fix the "rescaled" parameter value $\tilde{h}_z = h_z/(N^{-1} \sum_{j=1}^{N-1} \sum_{i>j} 1/|i-j|^{\alpha})$ to ensure consistent behavior across system sizes, where α is the exponent of the power-law interactions. As in Ref. [20], our initial state is the all-downs computational basis state: $|\downarrow,\ldots,\downarrow\rangle$. We use the rescaled parameters $(J_0,\tilde{h}_z,\alpha)=(1,0.7,1)$. In Fig. 1(e), we use on-site spin flip and dephasing errors: $\{\sigma_j^x,\sigma_j^z\}$, with a total error rate of $\gamma=0.05$ in a system of 16 qubits (with a total Hilbert space dimension of $2^{16}=65536$).

D. Rydberg blockaded model

We simulate a Rydberg blockaded model in two dimensions (2D), as recently experimentally realized in Ref. [21]. Here each site can be either in the ground $|\downarrow\rangle$ or Rydberg $|\uparrow\rangle$ state, subject to the constraint that there are no two adjacent Rydberg excitations $|\uparrow\rangle$. Its Hamiltonian is:

$$H_{\text{PXP}} = \Omega \sum_{j=1}^{N} PX_j + \delta \sum_{j} n_j , \qquad (S79)$$

with $PX_j \equiv \left[\bigotimes_{\langle i,j\rangle} |\downarrow\rangle\langle\downarrow|_i\right] \sigma_j^x$ the projected spin flip operator — a spin flip on site j is allowed only if all the nearest neighbors i of site j are in state $|\downarrow\rangle$.

We use the all-downs state $|\downarrow, \dots, \downarrow\rangle$ as our initial state. At zero detuning $\delta = 0$, this would be an infinite temperature state $(\langle H \rangle = tr(H)/D)$. Here we use the parameters $(\Omega, \delta) = (1, 0.7)$ to tune $|\downarrow, \dots, \downarrow\rangle$ away from infinite temperature. Furthermore, when $\delta = 0$, the Hamiltonian is particle-hole symmetric, leading to a different kind of universal behavior, detailed in Section V A. In Fig. 1(g), we use dephasing error $\{\sigma_j^z\}$ at a total error rate of $\gamma = 0.05$, in a 5 × 5 square grid of Rydberg atoms (with total Hilbert space dimension of 55447).

V. LIMITATIONS OF BENCHMARKING PROTOCOL: FAILURE CASES

As discussed in the main text, our benchmarking formula can fail when: 1) the k-th no resonance condition is not satisfied, 2) the effective dimension D_{β} is small, 3) the approach to equilibrium is slow, 4) the error is highly non-local, or 5) the readout basis states have well-defined symmetry quantum numbers. Below, we detail our findings for each case, and discuss alternate benchmarking formulae.

A. Violating the no-resonance condition: Particle-hole symmetry

The second no-resonance condition (S1) is extensively violated in the presence of a particle-hole symmetry (PHS). By this we mean a reflection symmetry in the spectrum: for every eigenvalue E, there is one at -E. For any given E, E', the equation $E_1 - E_2 + E_3 - E_4 = 0$ not only has solutions $(E_1, E_2, E_3, E_4) = (E, E, E', E')$ and (E, E', E', E), but also has solutions: $(E_1, E_2, E_3, E_4) = (E, -E, E', -E')$, (E, -E, -E', E'). This will give rise to additional terms in the second Hamiltonian twirling identity [Eq. (S2)]:

$$\mathbb{E}_{t} \left[U_{t}^{\otimes 2} A U_{-t}^{\otimes 2} \right]$$

$$\approx \sum_{E,E'} \left[|E, E' \rangle \langle E, E'| A | E, E' \rangle \langle E, E'| + |E, E' \rangle \langle E, E'| A | E', E \rangle \langle E', E| + |E, -E \rangle \langle E, -E| A | E', -E' \rangle \langle E', -E'| \right],$$
(S80)

suppressing the subleading collision terms. This can arise from, an anti-unitary charge conjugation operator, for example. Here, we focus on a simpler example. PHS is present in the PXP model with no detuning ($\delta = 0$): $H_{\text{PXP}} = \sum_{j} PX_{j}$. H_{PXP} anticommutes with the unitary operator $\mathcal{C} \equiv \prod_{j} \sigma_{j}^{z}$: $\mathcal{C}H_{\text{PXP}}\mathcal{C} = -H_{\text{PXP}}$ [22]. This symmetry is present in arbitrary dimensions— we will present numerical evidence for the two dimensional PXP model.

The PXP model is particularly convenient, for a number of reasons:

- (i) The computational basis states $|z\rangle$ are eigenstates of \mathcal{C} : $\mathcal{C}|z\rangle = \pm |z\rangle$. This implies that easily-prepared bitstring initial states such as $|\Psi_0\rangle = |\downarrow \dots \downarrow\rangle$ are also eigenstates of \mathcal{C} .
- (ii) H_{PXP} is real and thus possesses a time-reversal symmetry: $H_{\text{PXP}} = H_{\text{PXP}}^*$. In particular, its eigenstates are real in the computational basis.

The breakdown of the second no-resonance condition can be seen when we compute the time average of $P^{(2)}(t) = \sum_{z} p_{\text{avg}}(z)\tilde{p}(z,t)^2$:

$$\mathbb{E}_{t}\left[F_{\mathrm{id,d}}(t)\right] \approx \sum_{z} \left[2\left(\sum_{E} \left|\left\langle z|E\right\rangle \left\langle E|\Psi_{0}\right\rangle\right|^{2}\right)^{2} + \left|\sum_{E} \left\langle z|E\right\rangle \left\langle z|E\right\rangle \left\langle E|\Psi_{0}\right\rangle \left\langle -E|\Psi_{0}\right\rangle\right|^{2}\right] / p_{\mathrm{avg}}(z) \ . \tag{S81}$$

Using properties (i) and (ii) above, $\sum_E \langle z|E\rangle \langle z|-E\rangle \langle E|\Psi_0\rangle \langle -E|\Psi_0\rangle = p_{\rm avg}(z)$ and we obtain $\mathbb{E}_t\left[F_{\rm id,d}(t)\right]\approx 3$ instead of the usual value of two. This is illustrated in Fig. S6(a). We note that this result is contingent on conditions (i) and (ii) above — if these conditions were not satisfied, $\mathbb{E}_t\left[F_{\rm id,d}(t)\right]$ will have a non-universal value between two and three. For example, if we use an initial state that is *not* particle-hole symmetric, such as a low-energy Boltzmann state, $\mathbb{E}_t\left[F_{\rm id,d}(t)\right]\approx 2$, and F_d remains valid.

In particular, this implies that our F_d formula will not estimate the fidelity. Applying our simplifying assumptions in Eq. (S32), we obtain: $F_d \approx \frac{4}{3}F - \frac{1}{3}$. Instead, a modified formula should be employed:

$$F_d^{(PH)} = \frac{3}{2} \frac{\sum_z p_{\text{avg}}(z)\tilde{q}(z)\tilde{p}(z)}{\sum_z p_{\text{avg}}(z)\tilde{p}(z)^2} - \frac{1}{2} . \tag{S82}$$

However, a similar analysis reveals that F_e can be used with no modification. This is illustrated in Fig. S6(b).

1. Real Porter-Thomas distribution

The value of three above is the second moment of the real Porter-Thomas distribution [7] (stated, for simplicity, in the $D \to \infty$ limit):

$$P_{\text{PT},\mathbb{R}}(x) = \frac{\exp(-x/2)}{\sqrt{2\pi x}} \ . \tag{S83}$$

This distribution can be viewed as the overlap probability of a real-valued random vector $|\Psi\rangle$. It has k-th moments: $\int_0^\infty dx \ x^k P_{\text{PT},\mathbb{R}}(x) = (2k-1)!! \equiv (2k-1)(2k-3)\cdots 3\cdot 1$.

Intuitively, if both the initial state $|\Psi_0\rangle$ and $|z\rangle$ are even under \mathcal{C} , the overlap will be purely real: $\langle z|\Psi(t)\rangle=2\sum_{E\geq 0}\langle z|E\rangle\langle E|\Psi\rangle\cos(Et)$. We intuitively expect this to be a random variable and for $p(z,t)=|\langle z|\Psi(t)\rangle|^2$ to follow the real Porter-Thomas distribution. This also holds if $|\Psi_0\rangle$ or $|z\rangle$ are odd under \mathcal{C} .

We can prove that $\tilde{p}(z,t)$ (both with fixed time, and fixed configuration z) follows $P_{\text{PT},\mathbb{R}}$, assuming conditions (i) and (ii) above, and a particle-hole symmetric k no-resonance condition. The proof is identical to that of Theorem 2, except that instead only considering the permutations of k elements, we consider perfect matchings of 2k vertices. There are (2k-1)!! such perfect matchings, giving the desired k-th moments. We emphasize that to satisfy both conditions (i) and (ii), both time-reversal and particle-hole symmetry must be present in the Hamiltonian, and the initial state and readout basis states must have definite PHS parity.

B. Violating the no-resonance condition: Non-interacting models

The second no-resonance condition is also violated in non-interacting models. In non-interacting models, energy eigenvalues are given in terms of single-particle eigenvalues. For concreteness, consider a non-interacting Bose-Hubbard model, Eq. (S75) with U=0. Let the eigenvalues of the single-particle Hamiltonian be ϵ_k . An N-particle eigenstate is labelled by the occupation $\{n_k\}$ of the single-particle modes k, with energy $\sum_k n_k \epsilon_k$. This violates the 2 no-resonance condition: For any i,j,k,l, there are eigenvalues $E_1=\epsilon_i+\epsilon_j, E_2=\epsilon_k+\epsilon_l$ and $E_3=\epsilon_i+\epsilon_k, E_4=\epsilon_j+\epsilon_l$ such that $E_1+E_2=E_3+E_4$. Therefore, our Theorem does not apply to non-interacting models, reflected in Fig. S6(c). Consequently, neither F_d or F_e estimate the many-body fidelity (Fig. S6(d)). However, integrable and non-integrable dynamics may be quantitatively similar at short times, at which times the integrability breaking terms have not had sufficient time to appreciably change the dynamics. Since F_d is designed to work for these short quenches, F_d appears to estimate F in this case, as seen in Fig. S6(d).

C. Small effective dimension: Low temperature quench

Our protocol also breaks down when the effective dimension D_{β} is small. This happens in low temperature quenches, for example. In the extreme case that $|\Psi_0\rangle$ is an eigenstate, $D_{\beta}=1$. When $|\Psi_0\rangle$ is a low temperature state, it's dynamics are effectively constrained to a low-energy subspace. Following Theorem 2, in Fig. S6(e), the variable $\tilde{p}_z(t)$ approximately follows a Porter-Thomas distribution (S10) with the effective dimension of the outcome z, $D_{\beta}(z)$. Meanwhile, the distributions $\tilde{p}_t(z)$ show large fluctuations over time, again because of the small effective dimension.

Our protocol's systematic error and fluctuations scale inversely with D_{β} . Therefore, it is less applicable to low temperature quenches. In Fig. S6(f), we see a large discrepancy between F_d and F and large fluctuations over time. However, since the systematic error of F_e is less senstive to D_{β} (its $O(D_{\beta}^{-1})$ term vanishes), F_e estimates F, when averaged over a time window.

D. Slow equilibration: Quantum many-body scar states

Some many-body systems exhibit long-lived oscillations which delays equilibration of the quenched state. In the presence of these oscillations, normalizing the measurement outcomes p(z) with the equilibrium distribution $p_{\text{avg}}(z)$ gives incorrect estimators.

One prominent example of long-lived oscillations is the recent discovery of quantum many-body scar states [22, 23]. Originally experimentally discovered in a Rydberg quantum simulator, this phenomenon can be captured with the

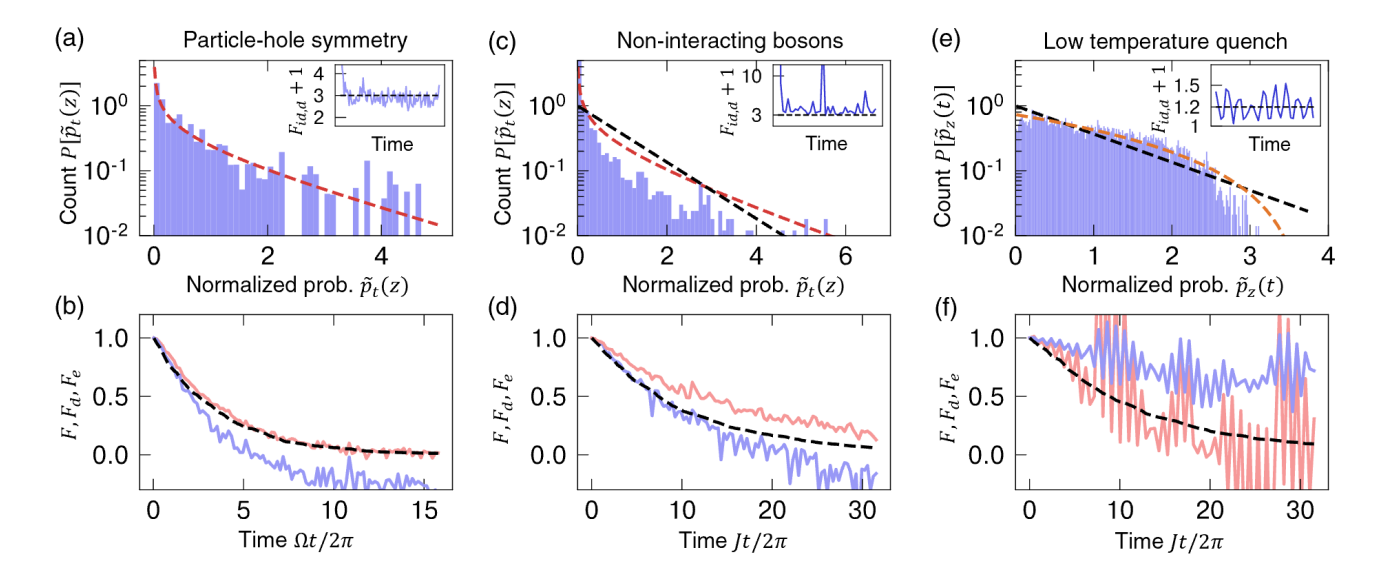


Figure S6. Failure cases of benchmarking protocol: Violation of no-resonance conditions and low effective dimension. (a) The particle-hole symmetry in the 2d PXP model violates the k no-resonance conditions (S1). Under special conditions (satisfied here in the 2d PXP model quenched from $|0\cdots 0\rangle$), $\tilde{p}(z,t)$ follows the real Porter-Thomas distribution, and $F_{\rm id,d}+1$ has an equilibrium value of 3 (inset). (b) The F_d formula (blue) breaks down, and must be modified as in Eq. (S82). In contrast, F_e (red) can be used without modification. (c) Non-interacting models also violate the no-resonance conditions. Here, we simulate a quench of the Bose-Hubbard model with no interaction U=0. The $\tilde{p}(z,t)$ follows neither PT distributions (red and black), and $F_{\rm id,d}+1$ has large temporal fluctuations (inset). (d) As a consequence, neither F_d nor F_e approximate F, although F_d is a good estimate at short times. (e) A low-temperature quench has a small effective dimension. We realize this with a Gibbs initial state $|\Psi_0\rangle = \sum_E \exp(-\beta/2E)|E\rangle$, with $\beta=4$ in a Bose-Hubbard model with 8 particles on 8 sites. $\tilde{p}_z(t)$, for an arbitrarily chosen z, follows a Porter-Thomas distribution with a small dimension (orange): here $D_{\beta}(z) \approx 3.75$. (f) As a consequence, F_d (blue) and F_e (red) have large temporal fluctuations, and F_d has a large systematic error. F_e is less susceptible to a small D_{β} , and is on average close to F.

1D PXP model:

$$H_{1\text{D-PXP}} = \Omega \sum_{j=2}^{L-1} P_{j-1}^{\downarrow} X_j P_{j+1}^{\downarrow} + X_0 P_1^{\downarrow} + P_{L-1}^{\downarrow} X_L + \delta \sum_j n_j , \qquad (S84)$$

where $P_j^{\downarrow} \equiv |\downarrow\rangle\langle\downarrow|_j$ is the projector onto the atomic ground state and $n_j \equiv |\uparrow\rangle\langle\uparrow|_j$ is the projector on the Rydberg excited state. A quench of the Neel state $|\downarrow\uparrow\downarrow\uparrow\cdots\downarrow\uparrow\rangle$ was observed to exhibit long-lived oscillations — in particular, persistent revivals of observables such as the magnetization and many-body fidelity. These are attributed to a tower of eigenstates, energy eigenstates with which $|\Psi_0\rangle$ has considerable overlap (Fig. S7(a), inset). Due to special properties of these eigenstates — most notably low half-chain entanglement entropy — these states are dubbed many-body scar states. While the phenomenon is most apparent with zero detuning, it persists with non-zero detuning. In our results in Fig. S7(a,b), we use a non-zero detuning $\delta = 0.2\Omega$ to break the particle-hole symmetry.

These revivals eventually decay in time. Therefore, $\tilde{p}_z(t)$ follows a PT distribution at late times (Fig. S7(a)). However, these long-lived oscillations are reflected in F_d and F_e (Fig. S7(b)) — F_d is a closer estimate to F than F_e .

E. Slow equilibration: Inhomogeneous initial state

If our initial state is strongly inhomogeneous, it will exhibit hydrodynamic oscillations before equilibrating [24]. At short times, the outcome probabilities $\tilde{p}(z,t)$ will be far from the relatively homogeneous $p_{\text{avg}}(z)$. We illustrate this with the initial state $|\Psi_0\rangle = |2,2,2,2,0,0,0,0\rangle$ on a Bose-Hubbard model with 8 bosons on 8 sites. We measure its relaxation with the average density in the left half $\langle n_L \rangle \equiv \langle n_1 + n_2 + n_3 + n_4 \rangle/4$, which exhibits decaying oscillations in Fig. S7(c). These oscillations are reflected in F_d and F_e , which show large deviations from F (Fig. S7(d)). We obtain better performance by normalizing p(z,t) and q(z,t) by a moving average $p'_{\text{avg}}(z) \equiv \int_{t-\Delta t/2}^{t+\Delta t/2} dt \ p(z,t)$, for a short interval Δt . We find that the modified F_e , $F'_e(t) \equiv (\sum_z p'_{\text{avg}}(z,t)\tilde{p}(z,t)-1)/(\sum_z p'_{\text{avg}}(z,t)\tilde{p}(z,t)^2-1)$ is a closer approximation to F.

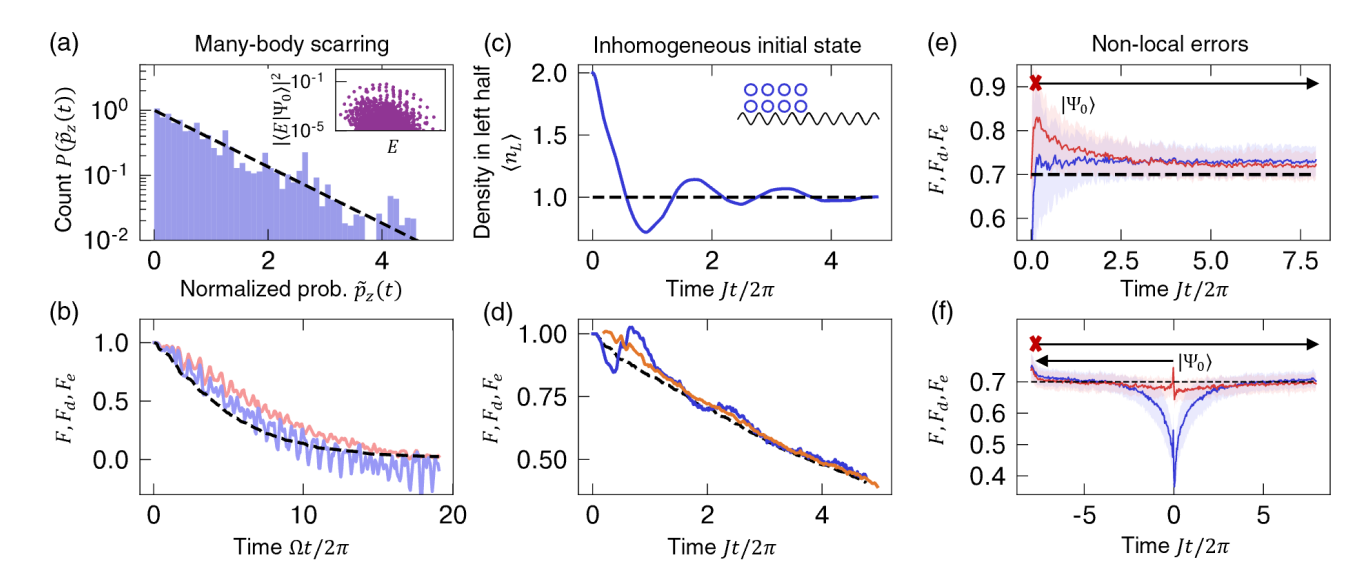


Figure S7. Failure cases of benchmarking protocol: Slow equilibration and non-local errors. (a) In the 1D PXP model, a quench of the Neel state $|\downarrow\uparrow\downarrow\uparrow\uparrow...\rangle$ undergoes slow thermalization due to large overlap with a "tower" of eigenstates (inset). $p_z(t)$ follows a PT distribution. (b) However, both F_d (blue) and F_e (red) show large oscillations and do not estimate F well (c) If an inhomogeneous state is quench evolved, it undergoes slow hydrodynamic relaxation, evidenced by the decaying oscillations of the average density in the left half of a Bose-Hubbard chain (blue). (d) Under this quench, both F_d (blue) and F_e (not plotted) exhibit oscillations. A modified F_e (orange) using a moving-averaged p_{avg} yields a closer estimate of the fidelity. (e) F_d and F_e response to an initial error. At short times F_d (blue) is a better estimate of F than F_e (red). Solid lines are average values over an ensemble of disordered Hamiltonians, with shaded areas indicating variance. (f) We apply a local error on a backward time-evolved state $|\Psi(-\tau)\rangle$ to engineer a non-local error on the initial state. In this case F_e (red) estimates F, while F_d (blue) does not, consistent with Appendix. III.

F. Non-local error on low entanglement states

In Appendix III, the random MPS model predicts that when the error size N_A is much smaller than the bond dimension χ , F_d is a better approximation to F at short times than F_e . This condition is satisfied in typical open system dynamics, since χ grows exponentially in time will N_A only grows linearly in time.

To verify our claim, we apply a single error at the start of the quench (t = 0) and compute F_d and F_e . Averaging over a large number of Bose-Hubbard Hamiltonians with disordered hopping strengths, we verify that F_d on average estimates F at very short times (albeit with large variance) (blue, Fig. S7(e)), while F_e (red) has a longer relaxation time.

To engineer a situation in the opposite limit, where $\chi \ll N_A$, we backwards time-evolve the initial state, then apply the local error on $|\Psi(-\tau)\rangle$. We then forward evolve the ideal and perturbed states. When |t| is small, this is equivalent to a non-local error $V(t+\tau)$ on the low-entanglement states $|\Psi(t)\rangle$. In this regime, as predicted, F_d (blue, Fig. S7(f)) deviates from F—reaching a minimum value of 2F-1, consistent with Eq. (S65)—while F_e is close to F (red).

We emphasize that such a situation is unlikely to arise in practical situations, and therefore F_d is more appropriate for short time quench dynamics than F_e . We illustrate this in an example of target state benchmarking in Fig. S8(b).

G. Non-ergodicity due to symmetry and readout in symmetry-resolved basis

We lastly discuss another case where F_d does not estimate F in the presence of symmetry and a readout basis that has well-defined symmetry quantum numbers.

In the presence of a symmetry, quantum states ergodically explore the Hilbert space of their symmetry sector. In generic readout bases, the presence of such symmetries does not impede F_d . However, if every state in the readout basis belongs to one symmetry sector, F_d will not be able to detect relative phase errors, or phase decoherence, between the different symmetry sectors. Physically, we can understand this as non-ergodicity of certain information about the state: the phase information never propagates into the readout basis. Mathematically, this does not affect our Theorems 1 and 2. However, our ansatz that $\tilde{q}(z) = F\tilde{p}(z) + (1-F)\tilde{p}_{\perp}(z)$ is no longer valid. Instead, consider two states, expressed as superpositions of states in different symmetry sectors: $|\Psi\rangle = \sum_j c_j |\Psi_j\rangle$ and $|\Psi'\rangle = \sum_j d_j |\Psi'_j\rangle$.

Then for a bitstring z in sector j, the ansatz should be modified to (assuming the quench processes for $|\Psi\rangle$ and $|\Psi'\rangle$ are identical):

$$\tilde{q}(z) = F_j \tilde{p}(z) + (1 - F_j) \tilde{p}_{\perp}(z) , \quad F_j \equiv \left| \left\langle \Psi_j \middle| \Psi_j' \right\rangle \right|^2$$
(S85)

Under this ansatz, F_d does not reproduce the true fidelity $F = \left|\sum_j c_j^* d_j \left\langle \Psi_j \middle| \Psi_j' \right\rangle \right|^2$. Applying our ansatz, and recalling that $p_{\text{avg}}(z) \equiv \mathbb{E}[p(z,t)]$, $F_{\text{XEB,d}} \equiv \sum_z p_{\text{avg}}(z) \tilde{q}(z) \tilde{p}(z) - 1$ takes the value $2 \sum_j |d_j|^2 F_j - 1$

Consider the simplest case, $|\Psi_j\rangle = |\Psi_j'\rangle$. Then $F_j = 1$, and $F_{\text{XEB,d}} = 2\sum_j |d_j|^2 - 1 = 1$, regardless of the value of c_j, d_j . Therefore, F_d is unable to estimate the fidelity. The infidelity arising from unequal populations $|c_j|^2$ of the symmetry sectors may be captured by a suitably modified formula. However, infidelity arising from different phases of c_j is intrinsically inaccessible from such measurements: if $d_j = \exp(i\theta_j)c_j$, then q(z) = p(z) identically.

Many analog simulators have readout bases that belong to a given symmetry sector. For example, itinerant particles in optical lattices readout configuration outcomes that have well-defined particle number, and their natural Hamiltonians also conserve particle number. However, states without well-defined particle number are not natural in such settings.

Such states that are in multiple symmetry sectors, however, may arise in other settings. Consider our trapped ion model $H_{\rm TI}$ (S78). This Hamiltonian conserves parity $\prod_j \sigma_j^z$, and the computational basis states have well-defined parity. Furthermore, it is easy to prepare states without well-defined parity: for example, one starts with the all-downs state $|\downarrow, \cdots, \downarrow\rangle$, and applies a local rotation on a single site. Therefore, such a family of states cannot be benchmarked with the F_d formula. As another example, such a scenario can arise in a spin chain, with a quench Hamiltonian that conserves magnetization $\sum_j \sigma_j^z$. Bitstrings in the computational basis have well-defined magnetization. In both cases, however, this can be remedied by measuring in the X-basis, in which outcomes do not have well-defined parity nor magnetization. This is explicitly demonstrated in a trapped-ion spin model in Fig. S8(e,f).

VI. GREEDY ALGORITHM FOR MULTIPARAMETER ESTIMATION

A. Algorithm

In this section we detail our greedy algorithm for simultaneous estimation of multiple Hamiltonian parameters, used in Fig. 4(c). Our algorithm is as follows. We are given a Hamiltonian $H(\boldsymbol{\theta})$ with n unknown parameters $\boldsymbol{\theta} = \{\theta_j\}_{j=1}^n$. We want to determine the actual experimental parameters $\{\theta_j^*\}$, assuming that we can prepare a fiducial state $|\Psi_0\rangle$ with high fidelity.

Our procedure is as follows:

- 1. Evolve $|\Psi_0\rangle$ for a fixed time.
- 2. Measure the configurations to approximate the distribution $q(z) = \langle z | \rho(t) | z \rangle$.
- 3. For some guess $\{\theta_i\}$, compute $p(z, \{\theta_i\}) = |\langle z| \exp(-iH(\{\theta_i\})t) |\Psi_0\rangle|^2$. Compute $F_d(\{J_i\})$.
- 4. Choose a random permutation $\pi \in S_n$. For each j, maximize $F_d(\{\theta_j\})$ over $\theta_{\pi(j)}$, keeping all other parameters fixed.
- 5. Repeat 4. for all $j = 1, \dots n$.
- 6. Repeat 3-5. until F_d converges.
- 7. Optionally repeat all steps with different initial guesses of $\{\theta_i\}$.

This procedure is justified as long as F_d does not vary too quickly in the range of $\{\theta_j\}$ considered.

In Fig. 4(c), we use this procedure to determine an unknown disorder potential atop a known systematic Hamiltonian. Our greedy algorithm works well as long as the disorder potential is small, and is also robust to errors in the experimental evolution.

VII. TARGET STATE BENCHMARKING

In Fig. 4(a) of our main text, we demonstrate target state benchmarking to determine the unknown phase of a GHZ-like state in a 2D array of Rydberg atoms. We take the prepared state to have a phase $\phi^* = \pi/4$. We wish

to measure ϕ^* by measuring the fidelity of the prepared state to target states with various values of ϕ . Using our protocol, we estimate the fidelity by measuring F_d after quench evolution.

In this section, we provide further demonstrations of target state benchmarking. We first consider the simplest setting of coherent local errors, which we demonstrate in the three other platforms studied. We then study benchmarking between states that are related by non-local deformations. We consider this setting for two applications: determining the Hamiltonian parameters corresponding to a ground state, as well as estimating the temperature of a low-energy state by measuring its overlap with the ground state.

A. Coherent local errors

Here, we demonstrate target state benchmarking in the Bose-Hubbard, Fermi-Hubbard, and trapped-ion spin chain model, using the same Hamiltonian and readout basis discussed in Section IV.

We consider locally rotated initial states: for the Bose-Hubbard model we consider a unity-filling Mott insulator state on 8 sites deformed by a local rotation ϕ on the middle two sites:

$$|\Psi(\phi)\rangle_{\rm BH} = \cos\phi |1, 1, 1, 1, 1, 1, 1, 1, 1\rangle + i\sin\phi |1, 1, 1, 2, 0, 1, 1, 1\rangle$$
 (S86)

For the Fermi-Hubbard model we consider the anti-ferromagnetic state with 8 particles on 8 sites, again rotated along the middle bond:

$$|\Psi(\phi)\rangle_{\rm FH} = \cos\phi |\uparrow,\downarrow,\uparrow,\downarrow,\uparrow,\downarrow,\uparrow,\downarrow\rangle + i\sin\phi |\uparrow,\downarrow,\uparrow,d,0,\downarrow,\uparrow,\downarrow\rangle , \qquad (S87)$$

where $d = \uparrow \downarrow$ denotes a doubly-occupied site, and 0 denotes an empty site. Lastly, for the trapped-ion model we consider the fully polarized state of 12 qubits, rotated by a pair of spin-flips across the middle bond

$$|\Psi(\phi)\rangle_{\text{TI}} = \cos\phi |\downarrow, \cdots, \downarrow, \downarrow, \downarrow, \cdots, \downarrow\rangle + i\sin\phi |\downarrow, \cdots, \downarrow, \uparrow, \downarrow, \cdots, \downarrow\rangle . \tag{S88}$$

A single bit-flip produces a coherent superposition across states with different parity. These states do not mix under the quench dynamics and the resulting fidelity cannot be estimated by F_d , if the readout basis is the computational basis. In contrast, if we measured in the X basis, F_d would be accurate, as discussed in (Section V G). If instead we had flipped two spins, our state would remain in the even-parity sector, and F_d would estimate F with any readout basis.

In all three cases, we compute the fidelity $F = |\langle \Psi(\phi^*) | \Psi(\phi) \rangle|^2 = \cos(\phi - \phi^*)^2$. In Fig. S8(a,c,e), we show that F_d , evaluated at a fixed point in time, estimates the fidelity F in all three cases. In Fig. S8(b,d,f), we show that F_d takes a short delay time to learn the value of F to a target state $\phi = \frac{\pi}{2}$ — only a relatively short quench evolution of t = O(1/J) is needed for this protocol. In the trapped ion model, F_d shows slightly larger deviations from F. This is because F_d fluctuates in time about F: this is indicated by the blue band in Fig. S8(e) and larger fluctuations Fig. S8(f).

B. Comparing non-locally deformed states

We next demonstrate verifying the preparation of a non-trivial ground state in two ways by computing the fidelities of states related by non-local deformations. We first demonstrate verifying the position in the phase diagram by computing the fidelities between a prepared critical ground state and the ground states of the same Hamiltonian at other parameter values. We then demonstrate estimating the temperature of the prepared state by considering a prepared low-temperature Boltzmann state of the Hamiltonian at the critical point and estimating its fidelity (overlap) to the ground state.

We simulate the ground state of the Bose-Hubbard model (S75) tuned to the Mott insulator-superfluid transition point at $(U/J)_{\rm crit} \approx 3.6$ on a system of 10 bosons on 10 lattice sites [25]. We wish to benchmark the fidelity of our prepared state against its desired ground state. We consider two purposes: estimating the best parameter U/J of the prepared ground state, and estimating the temperature of the prepared state.

To do so, we consider quench evolving our prepared state via a modified Bose-Hubbard Hamiltonian, and comparing it to simulated data of quenched ground states at various values of U/J. Here, care must be taken for two reasons. Firstly, the quench Hamiltonian should be chosen such that the ground states under investigation do not have too low energy with respect to the quench Hamiltonian. Secondly, the family of states we consider do not simply differ by local errors. Rather, the family of ground states are related by possibly non-local transformations. This is outside of the scope of our heuristic derivation. However, we numerically observe that the F_d formula still approximates F under judicious choices of the quench Hamiltonian.

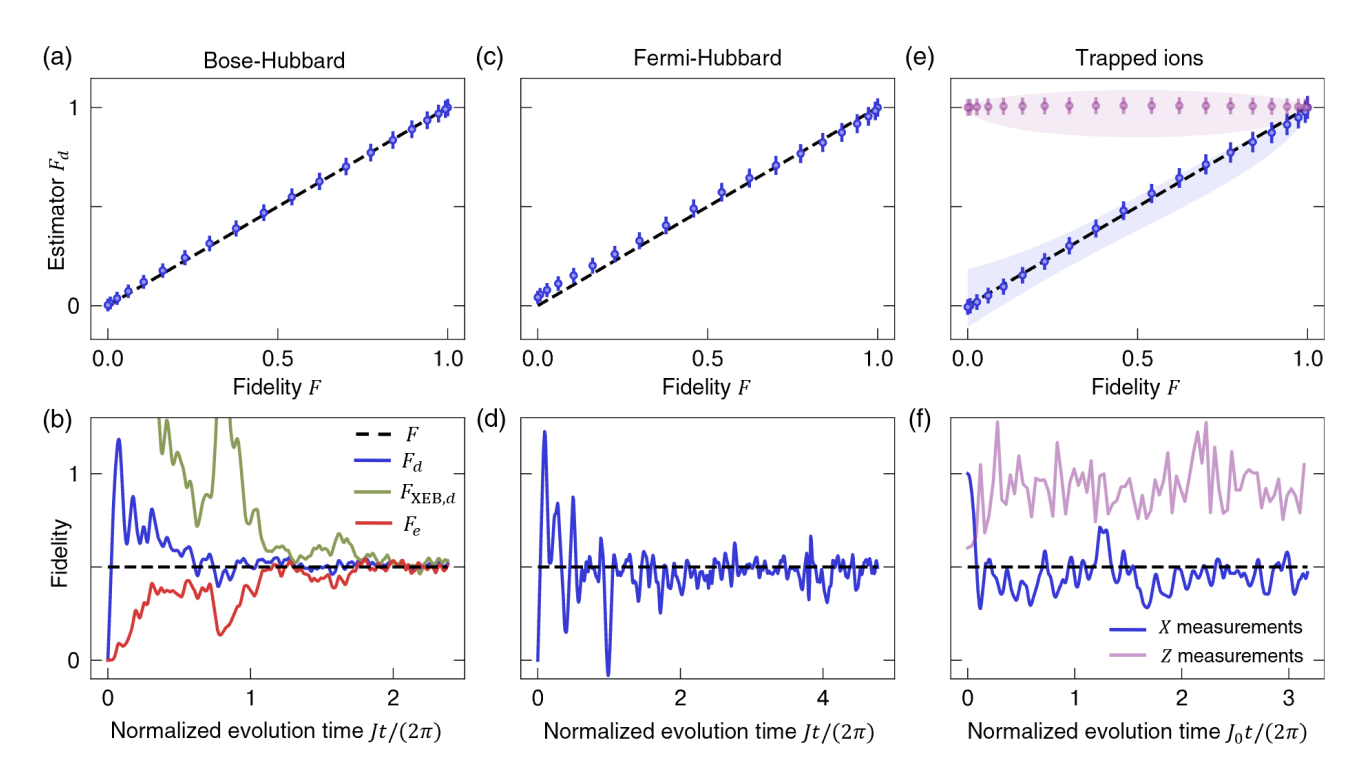


Figure S8. Target state benchmarking of locally-perturbed states. We apply local perturbations to initial states in a (a,b) Bose-Hubbard, (c,d) Fermi-Hubbard, and (e,f) trapped-ion spin chain model. We consider a class of states parametrized by an angle ϕ . We take states with $\phi^* = \pi/4$ as the simulated prepared state, and compare it to target states with variable ϕ . As a function of ϕ , the fidelity between the prepared and target states vary from 0 to 1. By quench evolving these states, we estimate their fidelity with F_d . In the top row, we demonstrate that the estimator F_d at a fixed, sufficiently late time, faithfully reproduces the fidelity F. Error bars denote the statistical uncertainty from a finite number M=1000 of samples. In the bottom row, we demonstrate the required evolution time for F_d to learn the true fidelity F, with the target state at $\phi=\pi/2$. In (b), we compare the different estimators discussed in the text: F_d (blue), F_e (green), and $F_{\text{XEB,d}}$ (red) in a Bose-Hubbard model. The difference between $F_{\text{XEB,d}}$ and F_d highlights the role of the denominator $\sum_z p_{\text{avg}}(z)\tilde{p}(z)^2$ at short times. In (e), we show that evaluating F_d at a fixed time shows slight deviations from F. This is due to the small effective dimension $D_{\beta} \approx 11$ in our trapped ion model: F_d fluctuates about F over time, as seen in (f) and indicated with the blue shaded region in (e). The purple markers and shaded regions in (e,f) indicate readout in the computational basis. Due to constraints from symmetry, F_d does not estimate F (in fact, it is constant in our setting). In (f), the purple curve is evaluated with a target state at $\phi = \pi/2 + \varepsilon$ for a small ε . This is because the target state at $\phi = \pi/2$ occupies only one out of two symmetry sectors, hence is a fine-tuned, pathological case.

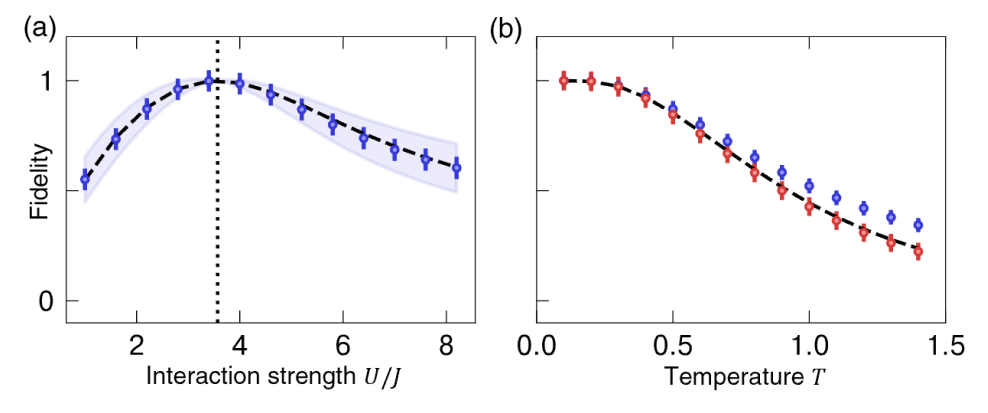


Figure S9. Target state benchmarking by verifying preparation of a ground state in a system. We consider two tasks: (a) estimating the corresponding parameter value and (b) estimating the temperature of the prepared state. In (a), we estimate the fidelity of the prepared state — assumed to be the ground state at the critical value of $(U/J)_{\rm crit} \approx 3.6$ — against the ground states at various values of U/J. We find that F_d (blue markers) is close to the true fidelity F (dashed line). The blue shaded region indicates the size of fluctuations of F_d over time. In (b), we estimate the fidelity of the prepared state — assumed to be the Boltzmann state at various temperatures T — against the ground state at $(U/J)_{\rm crit}$. We find that F_d (blue) slightly over-estimates F, while F_e (red) closely estimates F, consistent with our analysis in Section. II. In both plots, error bars indicate the statistical uncertainty associated with 1000 measurement samples.

In order for the ground states in both phases to have sufficiently ergodic quench dynamics, we consider a quench with a disordered Hamiltonian: $H = H_{\rm BH} \left[(U/J)_{\rm crit} \right] + \sum_{j=1}^{8} \Delta_j n_j$, where $\Delta_j \sim {\rm Unif}[-3,3]$. In Fig. S9(a), F_d approximates the true ground state overlap in a system of 8 bosons on 8 lattice sites.

We next demonstrate estimating the temperature of an experimentally prepared state. Assuming we have correctly determined the parameter U/J, we simulate the F_d values between the quench-evolved ground state and quench-evolved Boltzmann states $\rho = Z(T)^{-1} \exp(-H_{\rm BH}/T)$, where Z(T) is the partition function at temperature T. The fidelity is simply $Z(T)^{-1} \exp(-E_0/T)$. In this case, F_d [Fig. S9(b), blue], is close to the true fidelity. However, because of a relatively small effective dimension $D_\beta \approx 5$, F_d is larger than F, consistent with the prediction in Eq. (S38). This systematic shift can be manually subtracted. Alternatively, the estimator F_e [Eq. (S66)] is more robust to small values of D_β and closely estimates the fidelity [Fig. S9(b), red].

- [1] P. Reimann, Foundation of statistical mechanics under experimentally realistic conditions, Phys. Rev. Lett. **101**, 190403 (2008).
- [2] N. Linden, S. Popescu, A. J. Short, and A. Winter, Quantum mechanical evolution towards thermal equilibrium, Phys. Rev. E 79, 061103 (2009).
- [3] K. Kaneko, E. Iyoda, and T. Sagawa, Characterizing complexity of many-body quantum dynamics by higher-order eigenstate thermalization, Phys. Rev. A 101, 042126 (2020).
- [4] Y. Huang, Extensive entropy from unitary evolution, arXiv:2104.02053 (2021).
- [5] C. Dankert, R. Cleve, J. Emerson, and E. Livine, Exact and approximate unitary 2-designs and their application to fidelity estimation, Phys. Rev. A 80, 012304 (2009).
- [6] D. Gross, K. Audenaert, and J. Eisert, Evenly distributed unitaries: On the structure of unitary designs, Journal of mathematical physics 48, 052104 (2007).
- [7] C. E. Porter and R. G. Thomas, Fluctuations of nuclear reaction widths, Phys. Rev. 104, 483 (1956).
- [8] A. J. Short, Equilibration of quantum systems and subsystems, N. J. Phys. 13, 053009 (2011).
- [9] J. M. Deutsch, Eigenstate thermalization hypothesis, Rep. Prog. Phys. 81, 082001 (2018).
- [10] A. M. Dalzell, N. Hunter-Jones, and F. G. S. L. Brandão, Random quantum circuits transform local noise into global white noise, arXiv:2111.14907 (2021).
- [11] X. Gao, M. Kalinowski, C.-N. Chou, M. D. Lukin, B. Barak, and S. Choi, Limitations of linear cross-entropy as a measure for quantum advantage, arXiv:2112.01657 (2021).
- [12] B. Collins and I. Nechita, Random matrix techniques in quantum information theory, Journal of Mathematical Physics 57, 015215 (2016).
- [13] A. Nahum, S. Vijay, and J. Haah, Operator spreading in random unitary circuits, Phys. Rev. X 8, 021014 (2018).
- [14] V. Khemani, A. Vishwanath, and D. A. Huse, Operator spreading and the emergence of dissipative hydrodynamics under unitary evolution with conservation laws, Phys. Rev. X 8, 031057 (2018).
- [15] D. Jaksch, C. Bruder, J. I. Cirac, C. W. Gardiner, and P. Zoller, Cold bosonic atoms in optical lattices, Phys. Rev. Lett. 81, 3108 (1998).
- [16] A. J. Daley, Quantum trajectories and open many-body quantum systems, Adv. Phys. 63, 77 (2014).
- [17] H. Pichler, A. J. Daley, and P. Zoller, Nonequilibrium dynamics of bosonic atoms in optical lattices: Decoherence of many-body states due to spontaneous emission, Phys. Rev. A 82, 063605 (2010).
- [18] F. H. Essler, H. Frahm, F. Göhmann, A. Klümper, and V. E. Korepin, *The one-dimensional Hubbard model* (Cambridge University Press, 2005).
- [19] S. Sarkar, S. Langer, J. Schachenmayer, and A. J. Daley, Light scattering and dissipative dynamics of many fermionic atoms in an optical lattice, Phys. Rev. A 90, 023618 (2014).
- [20] J. Zhang, G. Pagano, P. W. Hess, A. Kyprianidis, P. Becker, H. Kaplan, A. V. Gorshkov, Z.-X. Gong, and C. Monroe, Observation of a many-body dynamical phase transition with a 53-qubit quantum simulator, Nature (London) 551, 601 (2017).
- [21] D. Bluvstein, A. Omran, H. Levine, A. Keesling, G. Semeghini, S. Ebadi, T. T. Wang, A. A. Michailidis, N. Maskara, W. W. Ho, et al., Controlling quantum many-body dynamics in driven rydberg atom arrays, Science 371, 1355 (2021).
- [22] C. J. Turner, A. A. Michailidis, D. A. Abanin, M. Serbyn, and Z. Papić, Quantum scarred eigenstates in a rydberg atom chain: Entanglement, breakdown of thermalization, and stability to perturbations, Phys. Rev. B 98 (2018).
- [23] H. Bernien, S. Schwartz, A. Keesling, H. Levine, A. Omran, H. Pichler, S. Choi, A. S. Zibrov, M. Endres, M. Greiner, et al., Probing many-body dynamics on a 51-atom quantum simulator, Nature (London) 551, 579 (2017).
- [24] R. Vasseur and J. E. Moore, Nonequilibrium quantum dynamics and transport: from integrability to many-body localization, J. Stat. Mech. 2016, 064010 (2016).
- [25] T. D. Kühner and H. Monien, Phases of the one-dimensional Bose-Hubbard model, Phys. Rev. B 58, R14741 (1998).